

1  
2  
3  
4  
5  
6  
7  
8  
9  
10  
11  
12  
13  
14  
15  
16  
17  
18  
19  
20  
21  
22  
23  
24  
25  
26  
27  
28  
29  
30  
31

## Magnetite-bubble aggregates at mixing interfaces in andesite magma bodies

M. Edmonds<sup>1\*</sup>, A. Brett<sup>1</sup>, R. A. Herd<sup>2</sup>, M. C. S. Humphreys<sup>3</sup>, A. Woods<sup>1</sup>

1. Earth Sciences Department, University of Cambridge, Downing Street, Cambridge CB2 3EQ

2. School of Environmental Sciences, University of East Anglia, Norwich

3. Earth Sciences Department, University of Durham

\* Corresponding author [me201@cam.ac.uk](mailto:me201@cam.ac.uk)

### **ABSTRACT**

Magnetite is a particularly favourable site for heterogeneous bubble nucleation in magma and yet only very rarely is evidence for this preserved, owing to the myriad of processes that act to overprint such an association. The possibility of bubble-magnetite aggregates in magmas carries with it interesting implications for the fluid mechanics of magma bodies and for the magma mixing process responsible for the formation of andesites. We use image analysis and statistical methods to illustrate a spatial association between magnetite and bubbles in mafic enclaves. There is a large range in magnetite contents in the enclaves, up to 7.5%, which is related to the porosity of the enclaves, indicating a mechanism of enrichment of the mafic magma in magnetite. In the andesite there is no spatial association between bubbles and magnetite and the magnetite content of the andesite is small. We suggest a mechanism for enclave formation whereby in vapour-saturated magma, bubbles nucleate on magnetite. Upon intrusion into the base of an andesite magma body, these bubble-magnetite aggregates rise and “sweep up” other magnetites, resulting in the accumulation of aggregates at the magma interface. Instabilities lead to the flotation of enclaves, characterised by enrichment in magnetite and bubbles.

32 There is strong evidence that mafic magmas in arc settings are rich in water. Rare olivine-hosted  
33 melt inclusions from Mount Shasta, for example, record H<sub>2</sub>O contents of up to 10 wt% (Grove et  
34 al., 2003) and data suggest that mafic arc melt inclusions have an average of 4 wt% H<sub>2</sub>O (Plank et  
35 al., 2013). Aluminium in hornblende hygrometers applied to arc mafic magmas require melt H<sub>2</sub>O  
36 contents of 4-8 wt% (Ridolfi et al., 2010). The H<sub>2</sub>O contents of the cores of pyroxene phenocrysts  
37 in equilibrium with andesite from Soufrière Hills Volcano reflect melt H<sub>2</sub>O contents of up to 10  
38 wt% (Edmonds et al., 2014), derived from the fractionation of a mafic melt with 4-6 wt% H<sub>2</sub>O.  
39 Models of "hot zone" processes at the base of the arc crust invoke water-rich magmas being  
40 emplaced into the lower crust, their outgassing lowering the solidus of the ambient crust and  
41 allowing assimilation of amphibolite and previously emplaced intrusions, leading to the formation  
42 of evolved magmas (Annen et al., 2006). It is therefore likely that mafic magmas, during their  
43 ascent through the arc crust, are vapour-saturated for most of their passage, carrying with them a  
44 population of bubbles of a supercritical fluid containing substantial H<sub>2</sub>O. The dissolved and  
45 exsolved volatile budget of these mafic magmas is a dominant control on the mechanisms of  
46 magma mingling and/or mixing when these magmas underplate, or intrude evolved, long-lived  
47 crystal-rich magma bodies in arcs (Huppert et al., 1982, 1986; Bacon, 1986; Nakamura, 1995;  
48 Huber et al., 2010). Ultimately, the transfer of these volatiles to the overlying andesitic magmas,  
49 and subsequent outgassing prior to and during eruption, controls eruption style, the transport and  
50 segregation of metals, and the flux of volcanic gases into the atmosphere. Finding petrological  
51 records of exsolved vapour and the process by which mafic magmas interact with cooler evolved  
52 magma bodies is challenging (Wallace, 2001; Blundy and Cashman, 2008; Gardner, 2009). Original  
53 bubble populations tend to be overprinted in stored and erupted magmas by crystallisation, bubble  
54 growth and coalescence, and outgassing (Larsen et al., 2004; Gardner, 2007). If, however, bubbles  
55 nucleate preferentially on one particular mineral phase, then this spatial association might provide a  
56 means to understand the fluid mechanics of bubbles, and of bubble-mineral aggregates in mafic arc  
57 magmas.

58  
59 Mafic magmas are likely to fractionate amphibole and magnetite throughout the arc crust (Sisson  
60 and Grove, 1993; Grove et al., 1982). It is likely, upon vapour saturation of the melt, that bubbles  
61 will nucleate on crystals that provide energetically favourable sites. During nucleation, the larger  
62 the liquid-mineral wetting angle (**figure 1**), the larger the reduction in surficial energy. In rhyolitic  
63 magmas, the liquid-mineral wetting angle for magnetite is 45-50°, compared with 5-25° for felsic  
64 silicates (Schafer and Foley, 2002; Gualda and Ghiorso, 2007). Nucleation on magnetite is therefore  
65 favoured over any other phase, in both theory and experiment. Extensive heterogeneous nucleation

66 of bubbles on magnetite has been observed during laboratory magma decompression experiments  
67 (Hurwitz and Navon, 1994; Mangan and Sisson, 2000, 2005; Gardner and Denis, 2004; Gardner,  
68 2007; Cluzel et al., 2008; Gardner and Ketcham, 2011). No such association between bubbles and  
69 other phases, such as quartz and feldspar, has been observed (Mangan and Sisson, 2000; Gualda and  
70 Ghiorso, 2007). It has been shown that the total Gibbs free energy of the bubble-liquid-crystal  
71 system is always lower in the case of bubble-crystal attachment over bubble-liquid configurations,  
72 meaning that heterogeneous nucleation is always preferred (Gonnerman and Gardner, 2013).  
73 Furthermore, as the wetting angle between bubble and mineral increases (**figure 1**), the efficiency  
74 of adhesion of bubbles to minerals is decreased (owing to the deformation force required to change  
75 the bubble shape from spherical) but the energy barrier to detachment of bubbles from crystals is  
76 greatly increased, so that once a bubble is attached, a larger force is required to detach it (Gualda  
77 and Ghiorso, 2007). The energy reduction caused by bubble-magnetite attachment is several orders  
78 of magnitude greater than that for bubble attachment to other minerals. Furthermore, it has been  
79 shown that, theoretically, magnetite grains of several hundred microns in size can be held attached  
80 to a bubble by surface forces (Gualda and Ghiorso, 2007).

81  
82 An association between magnetites and a bubble has been recognised previously: a pre-eruptive  
83 aggregate of multiple magnetite crystals and a single bubble was observed in a pumice sample from  
84 the Bishop Tuff rhyolite (Gualda and Anderson, 2007). This observation prompted suggestion that  
85 the formation of magnetite-bubble aggregates might be a mechanism of storing exsolved vapour in  
86 a magma reservoir, whereby the magnetite anchors the positively buoyant bubble (Gualda and  
87 Ghiorso, 2007). Finding evidence for such an association in erupted magmas is extremely  
88 challenging. Shear forces act to detach bubbles from crystals during eruption and during convection  
89 in the magma chamber. In addition, pre- and syn-eruptive processes of bubble growth, coalescence  
90 and outgassing will usually overprint the spatial link between the two phases, if such a link  
91 originally existed. Bearing in mind the ways in which overprinting of textures might occur, it would  
92 seem that the most likely magma types within which a spatial link between magnetite and bubbles  
93 might be preserved are those that quenched rapidly prior to eruption, such as mafic enclaves chilled  
94 against a cooler magma. In this scenario, enclaves may retain the characteristics of the original  
95 bubble and magnetite populations without significant modification.

96  
97 We studied samples erupted from Soufrière Hills Volcano, Montserrat in 2007. The eruption (1995-  
98 2011; Wadge et al., 2014) was characterised by crystal-rich andesite (with a rhyolitic melt), with up

99 to ~ 10 vol% mafic enclaves (Murphy et al., 2000; Barclay et al., 2010; Plail et al., 2014). The  
100 andesite exhibits petrological evidence for recent heating, in the form of sieve-textured plagioclase,  
101 opaticized amphibole, reverse-zoned orthopyroxene, and resorbed quartz (Murphy et al., 2000;  
102 Humphreys et al., 2009a). Melt inclusions in plagioclase in the andesite contain up to 6.3 wt% H<sub>2</sub>O  
103 and a few hundred ppm CO<sub>2</sub> (Humphreys et al., 2009b; Edmonds et al., 2014). Compositional  
104 zoning at the rims of titanomagnetite in contact with ilmenite suggests that at least the latest stage of  
105 heating might have taken place weeks-months before eruption (Devine et al., 2003). Geophysical  
106 observations of strain and ground deformation, as well as numerical modelling of magma flow,  
107 place constraints on the form of the plumbing system (Elsworth et al., 2008; Fooroozan et al., 2010;  
108 Hautmann et al., 2009). A coupled magma reservoir system exists at depth, with one magma storage  
109 area at around 12 km and one shallower, at around 5-7 km. The shallow chamber is connected to the  
110 surface via a dyke (Costa et al., 2013). Studies of volcanic gas emissions from Soufrière Hills  
111 Volcano have invoked largely unerupted mafic magma (perhaps the magma erupted in the form of  
112 enclaves) as the source of the sulphur gas emissions (Edmonds et al., 2001; 2010). Mafic enclaves  
113 have a diktytaxitic texture, indicative of rapid quenching against a cooler magma (Bacon 1986;  
114 Clyne, 1999; Martin et al., 2006) and a porosity of up to 40 vol% (Edmonds et al., 2014). Phase  
115 equilibria and amphibole compositions suggest water concentrations of up to 6-10 wt% (Edmonds  
116 et al., 2014). Mafic enclaves exhibit a range of textural and compositional types, ranging from  
117 basaltic enclaves with glassy margins to more crystalline enclaves of basaltic andesite composition  
118 (Plail et al., 2014).

119  
120 In this paper, we look for evidence that bubbles nucleate on magnetite in the magma reservoir  
121 beneath the Soufrière Hills Volcano. We use image analysis and statistical techniques on  
122 backscattered electron images to assess whether there is an association between magnetites and  
123 bubbles, or bubbles and other phases, in the erupted andesitic lavas and in mafic enclaves. We  
124 investigate the implications of such an association for understanding the behaviour of magnetite-  
125 bubble aggregates and magma mingling and the fluid mechanics of the basaltic magma at the  
126 interface with the andesite.

127

## 128 **METHODOLOGY**

129 We use statistical analysis of the spatial distribution of grains in 2D back-scattered electron images  
130 to investigate whether there is any relationship between the positions of magnetite grains and  
131 bubbles in the samples. Methods are described in detail below.

132

133 *Samples*

134 Samples for this study are andesitic blocks with porosity of up to 25 vol% in pyroclastic flow  
135 deposits (**table 1**). The lava blocks were sampled from the January 2007 Belham River pyroclastic  
136 flow deposit. The lava blocks have mafic enclaves up to 25 cm in dimension but more commonly <  
137 5 cm (Plail et al., 2014; **figure 2**), with a porosity of up to 25 vol%. The andesite blocks have been  
138 degassed to variable degrees and the porosity structure has been affected undoubtedly by bubble  
139 coalescence, outgassing and collapse (Klug and Cashman, 1996; Giachetti et al., 2010). The mafic  
140 enclaves, however, display glassy quenched rims and porosities up to 25 vol% (Edmonds et al.,  
141 2014), raising the possibility that they preserve a greater proportion of their original porosity  
142 structure that existed prior to eruption. The sample names have a hierarchy that relate to individual  
143 hand specimens from blocks in the flow deposit, i.e. BR6\_x where x is 1, 2 and 3 are three samples  
144 from the same hand specimen. Pumice samples were not used in this study as the exceedingly high  
145 vesicularity meant that crystals were too sparse and bubbles not separated sufficiently for  
146 meaningful statistical analysis.

147

148 *Scanning electron microscope images and image analysis*

149 The images were acquired using a JEOL JSM-820 Scanning Electron Microscope (SEM) operating  
150 at an accelerating voltage of 20kV (Earth Sciences, Cambridge). The software ImageJ was used to  
151 characterise the resulting images. Magnetite and vesicles were isolated by setting appropriate  
152 greyscale value thresholds, which were then quantified using the "Analyze Particles" function. For  
153 every particle, area (minimum, mean and maximum grey values), centroid, centre of mass, and  
154 perimeter length were recorded. Measurements were made with two minimum particle sizes (areas  
155 of 10 pixel units and 50 pixel units). The 10 px-thresholded analyses contained many more spurious  
156 results (e.g. of cracks or dust). As a consequence, the 50 px-thresholded analyses were used for the  
157 statistical analysis, which introduced a systematic failure to sample the smallest particles. However,  
158 the choice of this larger minimum size meant that most of the cracks and holes inside phenocrysts  
159 were avoided. There remains a small fraction of these voids in the interior of crystals (<<1% of total  
160 particles) that have been recorded as points in the populations, but these do not change the form of  
161 the statistical plots. Sampling bias was also introduced by the size of the thin sections: there is a  
162 potential bias away from the very largest vesicles, which exceed 0.5 cm in size. The backscatter  
163 images also vary in their magnification, resulting in a variable pixel size ranging from 0.14 microns  
164 to 2.25 microns (**table 1**), which may also affect results. The centroid positions of orthopyroxenes

165 was also recorded for sample MVO1560\_1 to test the null hypothesis that bubbles are related  
166 equally well spatially to all phases. Representative backscatter images of the andesite and of the  
167 mafic enclaves, with the phases labelled, are shown in **figure 3**.

168

### 169 *Statistical analysis*

170 The aim of the statistical analysis is to evaluate whether two populations are spatially clustered i.e.  
171 whether their locations are dependent upon one another. In the petrological literature, there are  
172 many examples of studies aiming to assess clustering and the spatial characteristics of single  
173 populations of phases (e.g. Jerram et al., 1996; Jerram et al., 2003; Higgins and Chandrasekharam,  
174 2007); far fewer attempting to assess the spatial dependence of multiple populations of phases. The  
175 traditional statistic used to evaluate clustering is the aggregation index,  $R$ , of Clark and Evans  
176 (1954) and later Kretz (1966), Boorman et al (2004), Higgins (2006) and Jerram et al. (1996, 2003).  
177 The  $R$  index is based on the nearest neighbour distances:

178

$$179 \quad R = \frac{r_A}{r_E} \quad (1)$$

180

181 where  $r_A$  is the mean of the distances separating points from their nearest neighbours, and  $r_E$  is the  
182 expected value of  $r_A$  for complete spatial randomness. By definition,  $R=1$  for complete spatial  
183 randomness. If the points are clustered, the distance to nearest neighbours is shorter than that  
184 expected for complete spatial randomness and  $R<1$ . Conversely, if points are ordered (with points  
185 further away than expected for spatial randomness),  $R>1$ . The nearest neighbour distance  
186 distribution function of a point pattern is the cumulative distribution function  $G(r)$  of the distance  
187  $r$  from a typical random point to the nearest other point of the population, given by

188

$$189 \quad G(r) = 1 - \exp(-\lambda\pi r^2) \quad (2)$$

190

191 where  $\lambda$  is the intensity, or the number of points per unit area. The drawback of using the  $R$  index,  
192 and nearest neighbor statistics, however, is that it is "short-sighted" and cannot characterise particle  
193 spatial patterns further away than the nearest neighbor. It cannot distinguish, for example, between  
194 complete spatial randomness and the case with both clustering and ordering on different length  
195 scales, since  $R=1$  in both cases (Rudge et al., 2008).

196

197 Instead of nearest neighbor analysis alone, we have chosen to use a range of statistical methods  
198 based on Ripley's K Function,  $K(r)$ , calculated using Spatstat, a statistical package that uses R as a  
199 platform. The pair correlation function (or radial distribution function)  $g(r)$  is defined as

200

$$201 \quad g(r) = \frac{1}{2\pi r} \frac{dK(r)}{dr} \quad (3)$$

202

203 where

204

$$205 \quad K(r) = \frac{E(\# \text{ extra events within distance } r \text{ of a randomly chosen event})}{\lambda} \quad (4)$$

206

207 and where  $\lambda$  is the number per unit area of particles. The parameter  $L(r)$ , a transformation of  
208  $K(r)$ , is defined as

209

$$210 \quad L(r) = \sqrt{\frac{K(r)}{\pi}} \quad (5)$$

211

212 For a completely random (uniform Poisson) point pattern, the theoretical value of the L-function is  
213  $L(r) = r$ , yielding a straight line with a positive slope on a plot of  $L(r)$  against  $r$  (e.g. **figure 4**).

214

215 The pair correlation function allows a more complex analysis of ordering and clustering on multiple  
216 length scales, instead of being confined to the nearest neighbour. The value  $g(r)$  determines how  
217 likely an inter-point distance of  $r$  is:  $g(r)$  is equal to 1 for complete spatial randomness. If  $g(r) > 1$   
218 then it is more frequent than complete spatial randomness; if  $g(r) < 1$  then it is less frequent than  
219 complete spatial randomness (e.g. **figure 4**). Edge effects are taken into account. These arise when  
220 incomplete grains near the edge, whose centroids fall within the bounding box, are not counted,  
221 leading to fewer grains near the edge, which biases all the statistics. Another source of error is that  
222 nothing is known about grains outside of the window under consideration: a grain may have a  
223 nearest neighbor just outside the window, for example, instead of the grains that are visible inside  
224 the window (Rudge et al., 2008). To correct for this latter effect, a buffer zone is introduced around

225 the edge of the observation window where nearest neighbour distances are not calculated, but the  
226 points are available as neighbours for the points in the inner region (Clark and Evans 1954). The  
227 buffer zone should be large enough so that the nearest neighbours of points in the inner region can  
228 always be found either in the inner region or in the buffer zone. Choosing the size of the buffer zone  
229 is critical: too large and valuable data is discarded; too small and edge effects remain (Rudge et al.,  
230 2008).

231

### 232 *Synthetic point patterns*

233 Synthetic distributions were generated to provide validation data for our investigation (**figures 4, 5**)  
234 and are divided into two groups. Independent populations (**figure 4**) are two separate populations (*A*  
235 and *B*) superimposed upon one another, where the individual points of each (*i* and *j*) have no spatial  
236 link or dependence; the populations may be random (poisson), clustered (gaussian) or ordered.  
237 Random populations were generated using a random number generator, with specified average  
238 intensity (point density). Clustered populations were generated using a number of random seed  
239 positions and specified cluster densities (we use "strong" and "weak" cluster densities with effects  
240 similar to those observed in natural distributions) and cluster dimensions, with a Gaussian  
241 distribution around the seed point. Ordered distributions are generated using a self-avoiding  
242 algorithm, whereby the image space is populated sequentially by points using the maximum  
243 distance from all existing neighbouring points.

244

245 For each synthetic point pattern, cumulative probability distributions to show nearest neighbour  
246 distances, Ripley's L function, and the pair correlation function, were generated (**figure 4**). For  
247 random population pairs that are not spatially linked (**figure 4a**), nearest neighbour cumulative  
248 probability plots show no difference from the data generated from the random simulations (grey  
249 envelope). For the rest of the independent pattern nearest neighbour plots, in general the nearest  
250 neighbour distances are longer than predicted for the random pair pattern simulations (i.e. there is a  
251 marked absence of short nearest neighbour distances), with the exception of random-ordered  
252 (**figure 4b**) and ordered-ordered (**figure 4e**), which show an absence of the longer distances,  
253 consistent with the ordering of at least one of the particle populations. In contrast, the plots of the  
254 cumulative Ripley's L Function shows that, without exception, when the two point patterns are  
255 spatially independent, regardless of point pattern "type" there is no statistical difference between  
256 simulations on two random point patterns, and the data generated from the synthetic pattern. The  
257 pair correlation function, which is essentially the non-cumulative form of the Ripley's L function,

258 shows essentially the same thing. The departures at small  $r$  reflect the nearest neighbour deviations  
259 from random behaviour. Importantly though, the medium and far-field are no different to the  
260 statistics generated from random simulations (the grey envelope), and this is true for all of the  
261 independent population point patterns in **figure 4**. The wave-like features at the larger distances  
262 have a wavelength proportional to cluster intensity, or ordering intensity. The only pattern showing  
263 a slightly stronger signal (a slight departure from random in Ripley's L function, and a positive  
264 excursion from random in the pair correlation function) is the synthetic pattern showing two  
265 independent clustering patterns (weak and strong; **figure 4i**). This may be an artefact arising from  
266 the particular point pattern generated. In order to establish the source of these data it would be  
267 necessary to run multiple analyses on a number of different clustering patterns. For the purposes of  
268 this analysis, however, it can be seen the departures from random for these independent population  
269 synthetic patterns in the medium and far field are small and of no consequence.

270

271 Linked, or dependent, populations are generated using common seed points (**figure 5**). For  
272 example, for a linked random-randomised two population synthetic pattern (**figure 5i**), population  $A$   
273 is a random (poisson) distribution of points  $i$ , population  $B$  is defined as having individual points  $j$   
274 ( $B_j$ ) shifted from  $A_i$ , using random vectors from each point  $i$ , using a specified number of pixels as  
275 available sites around  $A_i$ . For a linked ordered-clustered two population synthetic pattern, a random  
276 subset of the ordered point pattern points  $i$  of population  $A$  is used as seeds for the clusters in point  
277 pattern  $B$  defined by points  $j$ . Each point pattern contains 1000 points.

278

279 For each pair of dependent point patterns, statistical data for nearest neighbour, Ripley's L function,  
280 and the pair correlation function (pcf) were generated (**figure 5**). The statistical data show quite  
281 striking differences to the independent patterns shown in **figure 4**. Paired clustered populations  
282 have nearest neighbour cumulative probability distributions strongly skewed to small distances  
283 (**figure 5a-c**). Ordered-clustered paired populations show the opposite: distributions skewed to large  
284 distances, with the smallest distances absent (**figure 5d, e**). However, there are very large positive  
285 deviations at very small  $r$  ( $<0.1$ ), caused by the way that the second populations uses seeds derived  
286 from the first population. This strong positive deviation is observed in almost all of the dependent  
287 synthetic patterns and is also expected to occur in natural populations if they are strongly spatially  
288 linked. The ordered and random populations with the second population "randomised" around  
289 points of the first (**figure 5e, f**) show a larger fraction of smaller distances than the random case. For  
290 the Ripley's L function plots, which consider particles further away than the nearest neighbour,

291 significant departures from random behaviour are only observed when the two populations exhibit  
292 paired clustering, i.e. when the two populations are clustering in the same place (**figure 5a-c**). The  
293 pair correlation function shows positive and broad departures from random behaviour. The random-  
294 randomised results (a random first population, with the second population paired with it so that one  
295 particle of the second population is randomly distributed around each particle of the first; **figure 5i**)  
296 show an effect similar to the paired clustered populations above, albeit slightly weaker. There is a  
297 positive excursion from random in both nearest neighbour and Ripley's L function, and a similarly  
298 shaped pair correlation function plot (**figure 5i**). When one population is ordered, the pair  
299 correlation function plots show a negative deviation from random behaviour at distances of  $<1$ ,  
300 caused by the self-avoiding algorithm used to generate the ordered populations. This might arise in  
301 the natural population when there are other phenocrysts, for example, which act to separate the two  
302 populations in a systematic way, or when the two populations particle sizes have a finite minimum  
303 size.

304

305 The effect of changing the order of the analysis was also investigated (**figure 6**), for the cases of the  
306 dependent synthetic populations clustered-randomised and random-clustered. In the first case  
307 (**figure 6a**), the first population is clustered; this might represent clustered magnetites, for example.  
308 The second population nucleates preferentially upon the first, resulting in two clustered populations.  
309 This might represent bubbles nucleating on clustered magnetites, with the result being that  
310 magnetites and bubbles are both clustered, with common seed points. The spatial statistics show  
311 strong clustering in nearest neighbour distances, Ripley's L and the pair correlation function. In the  
312 second case, the first population is random and the second population nucleates preferentially upon  
313 the first. This represents the case where magnetites are distributed randomly and bubbles nucleate  
314 on them. The spatial statistics in this case are very different; clustering behaviour is only observed  
315 at small distances, with ordering at intermediate distances. These two cases might just as easily, of  
316 course, represent magnetites nucleating on clustered bubbles (**figure 6a**) and magnetites nucleating  
317 on randomly distributed bubbles (**figure 6b**). We regard this as slightly less likely than the case  
318 where magnetite is the first population. We can therefore discriminate, from the synthetic data,  
319 whether the first population is clustered or randomly distributed.

320

321 The results of these simulations show, unequivocally, that two independent populations can be  
322 distinguished from the case where the two populations are linked spatially. Furthermore, the nature  
323 of the linkage can be established in some cases: where both populations are clustered with common

324 seed points, this results in a very characteristic set of spatial statistics, most categorically in Ripley's  
325 L function. Comparison between the statistics generated from the natural data, with these results  
326 from the synthetic patterns, allows discrimination between these scenarios.

327

## 328 **RESULTS**

### 329 *Magnetite and vesicle size and area distributions*

330 Representative backscatter images of the vesicular andesite lava, breadcrust bombs and mafic  
331 enclaves are shown in **figure 3**. The size distributions of bubbles and magnetite grains are shown in  
332 **figure 7** as kernel density estimates (generated using the ksdensity normal kernel smoothing  
333 function in Matlab). The sample types (andesite or mafic enclave) are listed in **table 1** and marked  
334 on **figure 7**. In general, the vesicles in the mafic enclaves have larger modal sizes and broader size  
335 distributions, ranging to larger vesicle sizes. However, the more crystalline mafic enclaves (e.g.  
336 BR11, MVO 1592 1) have narrower peaks in the vesicle size distribution at smaller sizes, more  
337 similar to the andesite (**figure 7**). There are no clear differences in terms of magnetite size  
338 distribution between mafic enclaves and andesite samples. Modal bubble sizes range from 20-40  
339 microns, with some mafic enclave samples showing significant positive skew in the distribution,  
340 with tails extending up to 200-250 microns (e.g. MVO 1587 2, MVO 1592 4). Magnetite grains  
341 have a modal size of typically 25-60 microns, with the largest grains occurring in mafic enclave  
342 sample MT19 1. The grain size distributions are positively skewed, with a larger than expected  
343 proportion of larger crystals in the size range 100-300 microns. In almost all cases, the magnetite  
344 and vesicle sizes are coupled, such that the distributions show similar magnitudes and shapes for a  
345 single sample.

346

347 There is a large range in the area fraction of magnetite in the mafic enclave images, which reaches  
348 7.5 % (**figure 8**), which is in contrast to the andesite samples, which have magnetite area fractions  
349 up to *c.* 2 %. Vesicle area fractions range between 12 and 24 % in the mafic enclaves, and 2-23 % in  
350 the andesite samples. These values for vesicle area fraction are consistent with previous work for  
351 Soufrière Hills (Edmonds et al., 2014) and with work on bubble growth, outgassing and bubble  
352 collapse recorded in other similar dome-forming magmas (e.g. Stasiuk et al., 1996; Hammer et al.,  
353 2000; Scheu et al., 2006). There is a weak negative correlation between vesicle area fraction and  
354 magnetite area fraction (**figure 8**), which may indicate a genetic link between the two phases.

355

356 *Two population (bubble-magnetite) statistics*

357 **Figures 9, 10 and 11** show the point patterns and the statistics generated from the natural data,  
358 which are shown as backscatter images at the far left of the figure. Representative andesite samples  
359 are shown in **figure 9**, which shows, without exception, that there is no significant departure from  
360 random behaviour in the nearest neighbour plots. The large negative deviations at small  $r$  ( $<20$   
361 microns) are likely due to the finite size of the magnetites and vesicles (**figure 7**), which imposes  
362 ordering. All of the samples shown display a small positive deviation from random in the Ripley's  
363 L and pair correlation functions at distances 20-200 microns (**figure 9**), consistent with dependent  
364 clustering or dependent random populations (**figure 5**). The andesite pair correlation function data  
365 are isolated and shown in red in **figure 11**, with the theoretical random distribution shown at 1, as  
366 well as a grey envelope to show the region in which the results of 100 random simulations plot.  
367 Overall the statistical data for the andesite plots showing little near field and only weak medium  
368 field spatial linkage between magnetites and vesicles in the images.

369  
370 Representative data for the images that show parts of mafic enclaves are shown in **figure 10**. These  
371 data are markedly different from the andesite data in **figure 9**. Nearest neighbour plots consistently  
372 show a mode at higher distances than for the random case, characteristic of clustered populations,  
373 but not conclusive in showing that the populations are paired. However, the Ripley's L function  
374 plots for the enclaves show varying degrees of strong positive excursions from the random case,  
375 particularly for  $r < 100 \mu\text{m}$ , indicating that both populations are clustered (from comparison with  
376 **figure 5** and from the analysis shown in **figure 6**), and further, that they are spatially dependent  
377 upon one another, sharing common seed points. This paired, clustered relationship is also shown in  
378 the pair correlation function plots, which show a strong positive and broad shape. The comparison  
379 between the enclave and andesite pair correlation function with particle distance is shown in **figure**  
380 **11**. The data for the mafic enclaves are significantly different to the andesite and furthermore,  
381 significantly different from the envelope defined by the results of 100 random simulations, which is  
382 not the case for the andesite data. The mafic enclave pair correlation function plots also show  
383 negative deviations from random behaviour at  $r < 30$  microns, consistent with the bubble and  
384 magnetite sizes (**figure 7**), which imposes a minimum limit on particle separation and apparent  
385 ordering.

386  
387 To summarise, the statistical data for the mafic enclaves show that the first population of particles  
388 (magnetite) shows significant clustering, leading to linked clustered behaviour in the vesicle

389 distribution also. The andesite shows only a very weak spatial linkage between the two populations.  
390 The results of the pyroxene-bubble paired analysis are shown in **figure 12**. For this particular  
391 image, there is no spatial relationship between bubbles and orthopyroxene.

392

### 393 **DISCUSSION**

394 The results of this study show that magnetite and bubble sizes are coupled in all samples studied  
395 (**figure 7**). There is a large range in mafic enclave magnetite contents, which is related weakly to  
396 the vesicularity of the samples (**figure 8**). In the andesite samples, the area fraction of magnetite  
397 varies very little, up to 2%. We propose that the variation in vesicularity with magnetite content is  
398 linked with enclave bulk composition, as shown in previous studies (Edmonds et al., 2014; Plail et  
399 al., 2014). The enclaves may be classified into one of two types: A and B (Plail et al., 2014). Type  
400 A is more mafic in bulk composition (basaltic) and contains mainly hornblende and plagioclase as  
401 phenocryst phases. Vesicularity is high, the groundmass is glassy and the enclaves typically have  
402 quenched margins. The most vesicular enclaves in **figure 8**, with the lowest magnetite contents, are  
403 of this type. Type B enclaves range to basaltic andesite in bulk composition, and contain  
404 plagioclase, pyroxene and oxides as phenocryst phases. They have lower vesicularity and a  
405 crystalline groundmass, with no quenched margin; we propose that the lower vesicularity enclaves  
406 on **figure 8** are of this type. Type B enclaves have almost certainly lost a substantial portion of their  
407 porosity through outgassing, as suggested by their higher degree of bubble coalescence and absence  
408 of quenched glassy margins (Edmonds et al., 2014; Plail et al., 2014).

409

410 There is evidence of clustering in the mafic enclave samples, both within the single populations of  
411 magnetite and bubbles, and in the paired populations, which are spatially dependent upon one  
412 another. There is no evidence that bubbles are linked spatially with other crystal phases such as  
413 orthopyroxene (**figure 12**). In the andesite, however, there is no clear relationship and the  
414 populations are either independent or very weakly dependent. The individual populations are either  
415 random or slightly clustered, with varying degrees of ordering, likely imposed by the phenocryst  
416 phases present. The absence of a strong clustering between magnetites and bubbles in the andesite  
417 might be explained by overprinting of the association during magma ascent, degassing and  
418 rheological stiffening. We envisage that the shear forces generated during magma flow are likely to  
419 exceed the attachment forces between bubbles and magnetites, hence obliterating any association.  
420 The mafic enclaves are protected from such shear forces due to their coherence and their crystal  
421 frameworks, which makes them strong (Martin et al., 2006). Alternatively or in addition, the lower

422 magnetite content in the andesite might promote a greater proportion of bubble nucleation on other  
423 phases (Cluzel et al., 2008). We discuss the possible causes of the linked populations of bubbles and  
424 magnetite in the enclaves and the implications for the fluid mechanics of the system.

425

426 *The origin of magnetite-bubble aggregates in mafic arc magmas*

427 The clustering between magnetite and vesicles could be due to either magnetite nucleation on  
428 bubble walls, owing to short lengthscale changes in melt oxidation state and oxygen fugacity during  
429 degassing (Humphreys et al. in review; Moussallam et al. 2014), or to bubble nucleation on  
430 magnetite. Our results are consistent with both heterogeneous nucleation of bubbles on magnetite  
431 grains and a mechanism whereby bubbles "sweep up" magnetites during rise through melt. Of the  
432 crystal phases commonly present in arc settings, magnetite provides by far the most energetically  
433 favourable surface for heterogeneous nucleation of bubbles. Experiments show strong evidence for  
434 heterogeneous nucleation on all surfaces of magnetite, with no other minerals serving as nucleation  
435 sites during decompression (Gardner and Denis, 2004; Gardner, 2007; Cluzel et al. 2008; Gardner  
436 and Ketcham, 2011). Hurwitz and Navon (1994) developed a theoretical model of the relationship  
437 between liquid-mineral wetting angle and supersaturation, such that higher wetting angles favour  
438 heterogeneous over homogeneous nucleation. Gualda and Ghiorso (2007) show that in rhyolitic  
439 melts the attachment energy for magnetite-bubble aggregates is much greater than for silicate  
440 mineral-bubble aggregates. This is due to the significantly greater liquid-mineral wetting angles:  
441 45-50 degrees for magnetite, versus 5-25 degrees for felsic silicates (**figure 1**). The reduction in  
442 surface energy resulting from bubble-mineral attachment is at least one order of magnitude greater  
443 for magnetite than for any silicate mineral.

444

445 Clustering between magnetite and bubbles may be explained by heterogeneous nucleation of  
446 bubbles on magnetite, but also by bubbles "sweeping up" magnetites (**figure 13**; Belien et al.,  
447 2010). The latter mechanism involves rising bubbles coming into contact with magnetite grains: the  
448 reduction in surficial energy may be sufficient to stall the bubbles, with larger bubbles being split  
449 by the grains, which would influence their buoyancy. The range in total magnetite content would  
450 support this "sweeping up" mechanism, although this mechanism would intuitively lead to a  
451 positive correlation between vesicularity and magnetite content, which is not seen. It is likely,  
452 however, that these kinds of relationships would be very easily overprinted by outgassing of the  
453 magma during quenching and/or decompression.

454

455 *Implications of magnetite-bubble aggregates for the fluid mechanics of the system*

456 The presence of bubble-magnetite aggregates has fundamental implications for the degassing  
457 process by promoting heterogeneous over homogeneous nucleation, further favouring equilibrium  
458 degassing, low bubble number densities and affecting processes of bubble growth and coalescence  
459 (e.g. Gardner, 2009). Regardless of how bubble-magnetite aggregates form, their existence might  
460 also give rise to a number of complex behaviours in the magma reservoir. For example, if the  
461 overall bulk density of the magnetite-bubble aggregate is higher than the surrounding rhyolitic melt,  
462 the aggregate will sink (if the yield stress is overcome). Increasing pressure will tend to compress  
463 the bubble further, accelerating the aggregate's fall as a positive feedback mechanism. The system  
464 is possibly unstable in both directions so that some crystals may sink, and others may rise to the top  
465 of the chamber, depending on the pressure difference between top and base of chamber. If gas-  
466 crystal pairs are neutrally buoyant at some level in the magma chamber and are moved downwards,  
467 the pressure increase will cause bubble shrinkage and hence the density goes up fractionally and the  
468 aggregate will sink. Conversely if the aggregate rises a little, it will allow bubble expansion and the  
469 pair then becomes buoyant and will continue upwards. Hence it would not be possible dynamically  
470 to have an intermediate layer of bubble-crystals unless the surrounding melt is stratified (i.e. the  
471 density of fluid above the crystal-bubble pairs is lower by a finite amount and the density of the  
472 fluid below is greater). The presence of bubble-magnetite aggregates should therefore lead to  
473 magnetite-rich layers both at the floor and the roof of the chamber. Abundant clots of magnetite +  
474 orthopyroxene + apatite + vesicles ± plag exist in the andesite (Humphreys et al., 2009), perhaps  
475 remobilised from crystal mushes at the floor and roof of the magma chamber.

476

477 The large reduction in surficial energy available via formation of bubble-magnetite aggregates  
478 suggests that bubbles are extremely likely to attach to magnetite grains they interact with  
479 ("magnetite scavenging"). As bubbles rise they expand due to decompression, with further  
480 expansion due to bubble coalescence and continuing exsolution. The increase in rise speed due to  
481 increased buoyancy is counteracted by the greater likelihood of encountering more dense magnetite  
482 grains, which have the effect of slowing the aggregate down, and the greater difficulty of passing  
483 through the more crystal- and aggregate-rich magma. This mechanism might "trap" aggregates in  
484 regions of dense crystals ("mushes") and hence be a mechanism to store exsolved vapour, in the  
485 manner illustrated by the recent experiments of Belien et al., (2010).

486

487 In order to explain the links between bubbles and magnetites in the mafic enclaves, we propose the  
488 following conceptual model (**figure 13**) to explain our observations. Intruding mafic melts (>1000  
489 °C; Humphreys et al., 2009a) are significantly hotter than resident andesite magma (~830 °C,  
490 Humphreys et al., 2009a). If the mafic magma was H<sub>2</sub>O-rich, with >6 wt% H<sub>2</sub>O (on the basis of  
491 Rhyolitemelts modelling to reproduce the crystal assemblage; Edmonds et al., 2014), the mafic  
492 magma may have become vapour-saturated at >300 MPa in the arc crust. At this pressure  
493 magnetite, amphibole and orthopyroxene are likely liquidus phases (e.g. Davidson et al., 2007).  
494 Much of the bubble population would have nucleated on magnetite crystals. Upon intrusion into the  
495 base of the long-lived andesite magma reservoir (**figure 13**), bubble-magnetite aggregates were able  
496 to rise relative to the surrounding melt, as a consequence of both the low bulk viscosity of the melt  
497 and bubble expansion. The bubble-magnetite aggregates "swept up" more magnetite grains during  
498 their ascent, and the aggregates accumulated at the interface between the two magmas. There was  
499 probably little pervasive leakage and mixing between the two magmas owing to the large contrast in  
500 viscosity (Huppert et al., 1984, 1986; Phillips and Woods, 2001; 2002; Ruprecht et al., 2008),  
501 although the mafic magma, being around 150° C hotter than the andesite magma, quench  
502 crystallised to form the diktytaxitic texture characteristic of the enclaves (Murphy et al., 2000; Plail  
503 et al., 2014). A fraction of the vesicularity in the enclaves, perhaps a large fraction, is a result of  
504 quench crystallisation and vesiculation at the interface. Enclaves formed at the interface due to  
505 gravitational instabilities of the type proposed by Thomas et al. (1993). The enclaves preserved their  
506 magnetite and bubble-rich composition, as well as a texture indicating rapid crystallisation and  
507 further vesiculation at the interface. The range in magnetite contents probably reflects local  
508 variability in the concentration of aggregates at the interface; or perhaps reflects mixing with the  
509 host andesite in a "hybrid zone" at the interface, as suggested by Plail et al., (2014) to explain the  
510 geochemistry of the enclaves.

511

## 512 CONCLUSIONS

- 513 • We have used image analysis and statistical methods to illustrate a spatial association  
514 between magnetite and bubbles in the interior of mafic enclaves erupted in andesite lava  
515 blocks at Soufrière Hills Volcano. There is a large range in magnetite contents in the mafic  
516 enclaves, up to 7.5 % by volume, which is related to the porosity of the enclaves, indicating  
517 a genetic link between the two phases and a mechanism whereby enrichment of the mafic  
518 magma in magnetite occurs. In the crystal-rich andesite there is no or only a very weak  
519 spatial association between bubbles and magnetite. The total magnetite content of the  
520 andesite is lower (0.2-1.2 vol%).

- 521 • This study is the first to illustrate a statistical association between magnetite and bubbles in  
522 a volcanic rock and confirms the theoretical predictions which state that magnetite is a  
523 particularly favourable site for heterogeneous bubble nucleation in magma.
- 524 • The possibility of bubble-magnetite aggregates in magmas carries with it interesting  
525 implications for the fluid mechanics of magma chambers, involving the ability of magma  
526 bodies to “store” exsolved vapour, the formation of cumulates and crystal-rich mushes, and  
527 their remobilisation potential.
- 528 • We suggest a mechanism for enclave formation whereby water-saturated mafic magma  
529 nucleates bubbles on magnetite, which is a liquidus phase deep in the arc crust. Upon  
530 intrusion into the base of an andesite magma body, bubble-magnetite aggregates rise and  
531 “sweep up” other magnetite grains, resulting in the accumulation of bubbles and magnetite  
532 crystals at the magma interface. Instabilities lead to the flotation of enclaves, which are  
533 characterised by enrichment in magnetite and bubbles.

534

#### 535 **ACKNOWLEDGEMENTS**

536 Melissa Plail (University of East Anglia) supplied some of the mafic enclave samples used in this  
537 study. Rachel Ledden (University of Cambridge) acquired some of the backscattered electron  
538 images. MCSH acknowledges support from a Royal Society University Research Fellowship. We  
539 thank Caroline Martel and an anonymous reviewer for their comments, which improved the  
540 manuscript.

541

#### 542 **BIBLIOGRAPHY**

543 ANNEN, C., BLUNDY, J. D. & SPARKS, R. S. J. 2006. The genesis of intermediate and  
544 silicic magmas in deep crustal hot zones. *Journal of Petrology* 47, 3, 505–539.

545 BACON, C. R. 1986. Magmatic inclusions in silicic and intermediate volcanic rocks.  
546 *Journal of Geophysical Research, Solid Earth* B6, 6091–6112.

547 BARCLAY, J., HERD, R. A., EDWARDS, B., KIDDLE, E. & DONOVAN, A. 2010.  
548 Caught in the act: Implications for the increasing abundance of mafic enclaves during the eruption  
549 of the Soufrière Hills Volcano, Montserrat. *Geophysical Research Letters*, 37, 19.

550 BELIEN, I.B., CASHMAN, K.V. & REMPEL, A.W. 2010. Gas accumulation in particle-  
551 rich suspensions and implications for bubble populations in crystal-rich magma. *Earth and*  
552 *Planetary Science Letters*, 297, 133–140.

553 BLUNDY, J. & CASHMAN, K. V. 2008. Petrologic reconstruction of magmatic system  
554 variables and processes. *Reviews in Mineralogy and Geochemistry* 69, 1, 179–239.

555 BOORMAN, S., BOUDREAU, A., & KRUGER, F. J. 2004. The lower zone–critical zone  
556 transition of the Bushveld Complex: a quantitative textural study. *Journal of Petrology*, 45, 6,  
557 1209–1235.

558 CLARK, P.J. & EVANS, F.C. 1954. Distance to nearest neighbor as a measure of spatial  
559 relationships in populations. *Ecology*, 35, 445–453.

560 CLUZEL, N, LAPORTE, D., PROVOST, A. & KANNEWISCHER, I. 2008. Kinetics of  
561 heterogeneous bubble nucleation in rhyolitic melts: implications for the number density of bubbles  
562 in volcanic conduits and for pumice textures. *Contributions to Mineralogy and Petrology*, 156, 745–  
563 763.

564 CLYNNE, M. A. 1999. A complex magma mixing origin for rocks erupted in 1915, Lassen  
565 Peak, California. *Journal of Petrology* 40, 1, 105–132.

566 COSTA, A., WADGE, G., STEWART, R., & ODBERT, H. 2013. Coupled subdaily and  
567 multiweek cycles during the lava dome eruption of Soufrière Hills Volcano, Montserrat. *Journal of*  
568 *Geophysical Research, Solid Earth*, 118, 5, 1895–1903.

569 DAVIDSON, J., TURNER, S., HANDLEY, H., MACPHERSON, C. & DOSSETO, A.  
570 2007. Amphibole “sponge” in arc crust? *Geology* 35, 9, 787–790.

571 EDMONDS, M., AIUPPA, A., HUMPHREYS, M. C. S., MORETTI, R., GIUDICE, G.,  
572 MARTIN, R. S., HERD, R. A. & CHRISTOPHER, T. 2010. Excess volatiles supplied by mingling  
573 of mafic magma at an andesite arc volcano. *Geochemistry Geophysics Geosystems*,  
574 11:doi:10.1029/2009GC002781, 2010.

575 EDMONDS, M., HUMPHREYS, M. C. S., HAURI, E. H., HERD, R. H., WADGE, G.,  
576 RAWSON, H., LEDDEN, R., PLAIL, M., BARCLAY, J., AIUPPA, A., CHRISTOPHER, T.,  
577 GUIDICE, G. & GUIDA, R. 2014. Pre-eruptive vapour and its role in controlling eruption style and  
578 longevity at Soufrière Hills Volcano. In: *The eruption of Soufriere Hills Montserrat from 2000 to*  
579 *2010*. Eds G. Wadge, R. Robertson, B. Voight. Geological Society, London, *Memoirs*, 39, 289–313.

580 ELSWORTH, D., MATTIOLI, G., TARON, J., VOIGHT, B. & HERD, R. 2008.  
581 Implications of magma transfer between multiple reservoirs on eruption cycling. *Science*, 322,  
582 5899, 246–248.

583 GARDNER, J. E. & DENIS, M.-H 2004. Heterogeneous bubble nucleation on Fe-Ti oxide  
584 crystals in high-silica rhyolitic melts. *Geochimica et Cosmochimica Acta* 68, 17, 3587–3597.

585 GARDNER, J.E. 2007. Heterogeneous bubble nucleation in highly viscous silicate melts  
586 during instantaneous decompression from high pressure. *Chemical Geology* 236, 1, 1–12.

587 GARDNER, J.E. 2009. The impact of pre-existing gas on the ascent of explosively erupted  
588 magma. *Bulletin of Volcanology*, 71, 835–844.

589 GARDNER, J.E. & KETCHAM, R. A. 2011. Bubble nucleation in rhyolite and dacite melts:  
590 temperature dependence of surface tension. *Contributions to Mineralogy and Petrology*, 162, 929–  
591 943.

592 GONNERMANN, H. M. & GARDNER, J. E. 2013. Homogeneous bubble nucleation in  
593 rhyolitic melt: Experiments and nonclassical theory. *Geochemistry, Geophysics, Geosystems* 14,  
594 11, 4758–4773.

595 GROVE, T. L., ELKINS-TANTON, L. T., PARMAN, S. W., CHATTERJEE, N.,  
596 MÜNTENER, O., & GAETANI, G. A. 2003. Fractional crystallization and mantle-melting controls  
597 on calc-alkaline differentiation trends. *Contributions to Mineralogy and Petrology*, 145, 5, 515–533.

598 GROVE, T. L., GERLACH, D. M., & SANDO, T. W. 1982. Origin of calc-alkaline series  
599 lavas at Medicine Lake volcano by fractionation, assimilation and mixing. *Contributions to*  
600 *Mineralogy and Petrology* 80, 2, 160–182.

601 GUALDA, G. A. R. & ANDERSON, A. T. 2007. Magnetite scavenging and the buoyancy  
602 of bubbles in magmas. Part 1: Discovery of a pre-eruptive bubble in Bishop rhyolite. *Contributions*  
603 *to Mineralogy and Petrology*, 153, 733–772.

604 GUALDA, G. A. R. & GHIORSO, M. S. 2007. Magnetite scavenging and the buoyancy of  
605 bubbles in magmas. Part 2: Energetics of crystal-bubble attachment in magmas. *Contributions to*  
606 *Mineralogy and Petrology*, 154, 479–490.

607 HIGGINS, M. D. 2006. Verification of ideal semi-logarithmic, lognormal or fractal crystal  
608 size distributions from 2D datasets. *Journal of Volcanology and Geothermal Research*, 154, 1, 8–  
609 16.

610 Huber, C., Bachmann, O., & Manga, M. 2010. Two competing effects of volatiles on heat  
611 transfer in crystal-rich magmas: Thermal insulation vs defrosting. *Journal of Petrology* 51, 4, 847–  
612 867.

613 FOROOZAN, R., ELSWORTH, D., VOIGHT, B., & MATTIOLI, G. S. 2010. Dual  
614 reservoir structure at Soufrière Hills Volcano inferred from continuous GPS observations and  
615 heterogeneous elastic modeling. *Geophysical Research Letters*, 37, 19.

616 GIACHETTI, T., DRUITT, T. H., BURGISSER, A., ARBARET, L. & GALVEN, C. 2010.  
617 Bubble nucleation, growth and coalescence during the 1997 Vulcanian explosions of Soufrière Hills  
618 Volcano, Montserrat. *Journal of Volcanology and Geothermal Research*, 193, 215–231.

619 HAMMER, J. E., CASHMAN, K. V., & VOIGHT, B. 2000. Magmatic processes revealed  
620 by textural and compositional trends in Merapi dome lavas. *Journal of Volcanology and Geothermal*  
621 *Research*, 100, 1, 165–192.

622 HAUTMANN, S., GOTTMANN, J., SPARKS, R. S. J., COSTA, A., MELNIK, O. &  
623 VOIGHT, B. 2009. Modelling ground deformation caused by oscillating overpressure in a dyke  
624 conduit at Soufrière Hills Volcano, Montserrat. *Tectonophysics*, 471, 1, 87–95.

625 HIGGINS, M. D., & CHANDRASEKHARAM, D. 2007. Nature of sub-volcanic magma  
626 chambers, Deccan province, India: Evidence from quantitative textural analysis of plagioclase  
627 megacrysts in the Giant Plagioclase Basalts. *Journal of Petrology*, 48, 5, 885–900.

628 HUMPHREYS, M. C. S., CHRISTOPHER, T. & HARDS, V. 2009. Microlite transfer by  
629 disaggregation of mafic inclusions following magma mixing at Soufrière Hills Volcano, Montserrat.  
630 *Contributions to Mineral Petrology*, 157, 609–624.

631 HUMPHREYS, M. C. S., EDMONDS, M., CHRISTOPHER, T., & HARDS, V. (2009).  
632 Chlorine variations in the magma of Soufrière Hills Volcano, Montserrat: Insights from Cl in  
633 hornblende and melt inclusions. *Geochimica et Cosmochimica Acta*, 73, 19, 5693–5708.

634 HUMPHREYS, M. C. S., BROOKER, R. A., FRASER, D. G., BURGISSER, A.,  
635 MANGAN, M. T. & MCCAMMON, C. 2014. Iron oxidation state in hydrous rhyolites during  
636 magma ascent and degassing. *Journal of Petrology*, in review.

637 HUPPERT, H. E., SPARKS, R. S. J., WHITEHEAD, J. A., & HALLWORTH, M. A. 1986.  
638 Replenishment of magma chambers by light inputs. *Journal of Geophysical Research, Solid Earth*  
639 91, B6, 6113–6122.

640 HUPPERT, H. E., SPARKS, R. S. J., & TURNER, J. S. (1984). Some effects of viscosity on  
641 the dynamics of replenished magma chambers. *Journal of Geophysical Research: Solid Earth* 89,  
642 B8, 6857–6877.

643 HURWITZ, S. & NAVON, O. 1994. Bubble nucleation in rhyolitic melts: Experiments at  
644 high pressure, temperature and water content. *Earth & Planetary Science Letters*, 122, 267–280.

645 JERRAM, D. A., CHEADLE, M. J., HUNTER, R. H., & ELLIOTT, M. T. 1996. The spatial  
646 distribution of grains and crystals in rocks. *Contributions to Mineralogy and Petrology*, 125, 1, 60–  
647 74.

648 JERRAM, D. A., CHEADLE, M. J., & PHILPOTTS, A. R. 2003. Quantifying the building  
649 blocks of igneous rocks: are clustered crystal frameworks the foundation? *Journal of Petrology*, 44,  
650 11, 2033–2051.

651 KIDDLE, E. J. 2011. The structure of the crust and magmatic system at Montserrat, Lesser  
652 Antilles. PhD thesis, University of Bristol.

653 KLUG, C., & CASHMAN, K. V. 1996. Permeability development in vesiculating magmas:  
654 implications for fragmentation. *Bulletin of Volcanology*, 58, 2–3, 87–100.

655 KRETZ, R. 1966. Interpretation of the shape of mineral grains in metamorphic rocks.  
656 *Journal of Petrology*, 7, 1, 68–94.

657 LARSEN, J. F., DENIS, M.-H. & GARDNER, J. E. 2004. Experimental study of bubble  
658 coalescence in rhyolitic and phonolitic melts. *Geochimica et Cosmochimica Acta* 68, 2, 333–344.

659 MANGAN, M. & SISSON, T. 2005. Evolution of melt-vapor surface tension in silicic  
660 volcanic systems: experiments with hydrous melts. *Journal of Geophysical Research*, 110, B01202.

661 MARTIN, V. M., HOLNESS, M. B., & PYLE, D. M. 2006. Textural analysis of magmatic  
662 enclaves from the Kameni Islands, Santorini, Greece. *Journal of Volcanology and Geothermal  
663 Research*, 154, 1, 89–102.

664 MOUSSALLAM, Y., OPPENHEIMER, C., SCAILLET, B., GAILLARD, F., KYLE, P.,  
665 PETERS, N., HARTLEY, M., BERLO, K. & DONOVAN, A. 2014. Tracking the oxidation state of  
666 Erebus magmas, from mantle to surface, driven by magma ascent and degassing. *Earth and  
667 Planetary Science Letters* 393, 200–209.

668 MURPHY, M. D., SPARKS, R. S. J., BARCLAY, J., CARROLL, M. R. & BREWER, T. S.  
669 2000. Remobilization of andesite magma by intrusion of mafic magma at the Soufrière Hills  
670 Volcano, Montserrat, West Indies. *Journal of Petrology*, 41, 21–42.

671 NAKAMURA, M. 1995. Continuous mixing of crystal mush and replenished magma in the  
672 ongoing Unzen eruption. *Geology* 23, 9, 807–810.

673 PHILLIPS, J. C., & WOODS, A. W. 2002. Suppression of large-scale magma mixing by  
674 melt–volatile separation. *Earth and Planetary Science Letters* 204, 1, 4–60.

675 PHILLIPS, J. C. & WOODS, A. W. 2001. Bubble plumes generated during recharge of  
676 basaltic magma reservoirs. *Earth and Planetary Science Letters* 186, 2, 297–309.

677 PLAIL, M., BARCLAY, J., HUMPHREYS, M. C. S., EDMONDS, M., HERD, R. A. &  
678 CHRISTOPHER, T., 2014. Characterisation of mafic enclaves in the erupted products of Soufrière

679 Hills Volcano, Montserrat 1995-2010. In: The eruption of Soufriere Hills Montserrat from 2000 to  
680 2010. Eds G. Wadge, R. Robertson, B. Voight. Geological Society, London, Memoirs, 39, 341–358.

681 PLANK, T., KELLEY, K. A., ZIMMER, M. M., HAURI, E. H. & WALLACE, P. J. 2013.  
682 Why do mafic arc magmas contain ~ 4wt% water on average? Earth and Planetary Science Letters  
683 364, 168–179.

684 RIDOLFI, F., RENZULLI, A. & PUERINI, M. 2010. Stability and chemical equilibrium of  
685 amphibole in calc-alkaline magmas: an overview, new thermobarometric formulations and  
686 application to subduction-related volcanoes. Contributions to Mineralogy and Petrology 160, 1 45–  
687 66.

688 RUDGE, J. F., HOLNESS, M. B., & SMITH, G. C. 2008. Quantitative textural analysis of  
689 packings of elongate crystals. Contributions to Mineralogy and Petrology, 156, 4, 413–429.

690 RUPRECHT, P., BERGANTZ, G. W. & DUFEK, J. 2008. Modeling of gas-driven  
691 magmatic overturn: Tracking of phenocryst dispersal and gathering during magma mixing.  
692 Geochemistry, Geophysics, Geosystems 9, 7.

693 SCHÄFER, F. N. & FOLEY, S. F. 2002. The effect of crystal orientation on the wetting  
694 behaviour of silicate melts on the surfaces of spinel peridotite minerals. Contributions to  
695 Mineralogy and Petrology, 143, 254–261.

696 SCHEU, B., SPIELER, O., & DINGWELL, D. B. 2006. Dynamics of explosive volcanism  
697 at Unzen volcano: an experimental contribution. Bulletin of volcanology, 69, 2, 175–187.

698 STASIUK, M. V., BARCLAY, J., CARROLL, M. R., JAUPART, C., RATTÉ, J. C.,  
699 SPARKS, R. S. J., & TAIT, S. R. 1996. Degassing during magma ascent in the Mule Creek vent  
700 (USA). Bulletin of Volcanology, 58, 2-3, 117–130.

701 THOMAS, N., TAIT, S. & KOYAGUCHI, T. 1993. Mixing of stratified liquids by the  
702 motion of gas bubbles: application to magma mixing. Earth and Planetary Science Letters 115, 1  
703 161–175.

704 WADGE, G., VOIGHT, B., SPARKS, R.S.J., COLE, P., LOUGHLIN, S.C., 2014. An  
705 Overview of the Eruption of Soufrière Hills Volcano from 2000-2010. In: The eruption of Soufriere  
706 Hills Montserrat from 2000 to 2010. Eds G. Wadge, R. Robertson, B. Voight. Geological Society,  
707 London, Memoirs, 39.

708 WALLACE, P. J. 2001. Volcanic SO<sub>2</sub> emissions and the abundance and distribution of  
709 exsolved gas in magma bodies. Journal of Volcanology and Geothermal Research 108, 1, 85–106.

710

711 **FIGURE CAPTIONS**

712

713 **Figure 1:** Two possible configurations of bubble, liquid and crystal. On the left, the bubble is  
714 entirely within the liquid; on the right it is attached to the crystal. The schematic diagram of the  
715 melt-bubble-crystal junction indicates the balance of forces, with surficial energies ( $\sigma$ ), the wetting  
716 angle  $\Psi$  and the bubble-mineral angle  $\theta$ . Modified from Gualda and Ghiorso (2007).

717

718 **Figure 2:** Photographs of lava blocks in the field. Lava blocks were emplaced by a pyroclastic flow  
719 on 7 January 2007 from Soufrière Hills Volcano in the Belham River Valley, Montserrat. The  
720 blocks are a few metres in dimension (a), made of porphyritic andesite, with small mafic enclaves  
721 (shown in (b)) of basaltic to basaltic andesite composition. Hammer in (a) 47 cm long.

722

723 **Figure 3:** Representative backscattered electron images from the Scanning Electron Microscope: a-  
724 c show mafic enclaves, d shows porous andesite, all labelled with sample number. Phases are  
725 labelled: mgt: magnetite; ves: vesicle; amph: amphibole; opx: orthopyroxene; plag: plagioclase; gl:  
726 glass.

727

728 **Figure 4:** Synthetic point patterns to show two independent populations and their associated  
729 statistics. Left: point patterns to show the spatial arrangement of the two populations, each labelled  
730 with the characteristics of each population (random, clustered etc; described in text). Plots from left  
731 to right: cumulative probability distribution to show Nearest Neighbour Distances, in microns; a  
732 plot of Ripley's L Function against distance,  $r$ , in microns; the Pair Correlation Function against  
733 distance,  $r$ , in microns. Also shown in each plot, as grey shading, are the results of 100 random  
734 (poisson) point pattern simulations. Plots generated using the Spatstat package in R.

735

736 **Figure 5:** Synthetic point patterns to show two dependent populations and their associated statistics.  
737 Left: point patterns to show the spatial arrangement of the two populations, each labelled with the  
738 characteristics of each population (random, clustered etc; described in text). An explanation of how  
739 the second population is generated using seed positions from the first population is given in the text.  
740 Plots from left to right: cumulative probability distribution to show Nearest Neighbour Distances, in  
741 microns; a plot of Ripley's L Function against distance,  $r$ , in microns; a plot to show the Pair  
742 Correlation Function against distance,  $r$ , in microns. Also shown in each plot, as grey shading, are  
743 the results of 100 random (poisson) point pattern simulations. Plots generated using the Spatstat

744 package in R.

745

746 **Figure 6:** The effect of changing the order of the spatial analysis of the dependent populations in  
747 the case of clustered-randomised or random-clustered distributions: a) the first population is  
748 clustered and the second is linked spatially to the first, resulting in two clustered populations. The  
749 nearest neighbour, Ripley's L and pair correlation functions (described in the text) shown strong  
750 clustering; b) the first population is randomly distributed and the second is linked spatially to the  
751 first population, resulting in the second population being weakly clustered. The nearest neighbour,  
752 Ripley's L and pair correlation functions show clustering only on very small lengthscales and  
753 ordering at intermediate lengthscales.

754

755 **Figure 7:** Bubble and magnetite size distributions for all of the samples studied. Curves are labelled  
756 with sample name (Table 1) and sample type (andesite or mafic enclave). In general bubble size  
757 distributions are shown in black, magnetite size distributions in red.

758

759 **Figure 8:** Vesicle area fraction (% , y axis) plotted against vesicle-free magnetite area fraction (% , x  
760 axis). Andesite and mafic enclave samples are distinguished.

761

762 **Figure 9:** Representative statistical data for populations of magnetite and bubbles for a) one mafic  
763 enclave sample and b) to e) andesite samples. Plots from left to right: point pattern of bubbles  
764 (white) and magnetite (black), alongside the backscattered images of the analysed areas; Nearest  
765 Neighbour distances ( $G(r)$ ; black solid line) as a cumulative probability distribution with distance,  $r$   
766 in microns, showing distributions that lie inside the envelope (in grey) for 100 random simulations  
767 (red dashed line shows the results for a theoretical random distribution); Ripley's L Function with  
768 distance  $r$ ; the Pair Correlation Function with distance  $r$ .

769

770 **Figure 10:** Representative statistical data for populations of magnetite and bubbles for mafic  
771 enclave samples. Plots from left to right: point pattern of bubbles (white) and magnetite (black),  
772 alongside the backscattered images of the analysed areas; Nearest Neighbour distances ( $G(r)$ ; black  
773 solid line) as a cumulative probability distribution with distance,  $r$  in microns, showing distributions  
774 that lie inside the envelope (in grey) for 100 random simulations (red dashed line shows the results  
775 for a theoretical random distribution); Ripley's L Function with distance  $r$ ; the Pair Correlation  
776 Function with distance  $r$ .

777

778 **Figure 11:** Plot to show the pair correlation function (pcf) as a function of distance  $r$  (in microns)  
779 for all of the point patterns studied here, separated into their types: andesite (red) and mafic enclave  
780 (black). The horizontal black line shows the pcf for a theoretical random distribution, and the grey  
781 envelope, the result of 100 random simulations.

782

783 **Figure 12:** Statistical plots to show the relationship between the locations of pyroxenes and the  
784 locations of bubbles in sample MVO1560\_1. The plots show that there is no statistical departure  
785 from random behaviour, showing no linked spatial patterns. Plots as described in figures 9 and 10.

786

787 **Figure 13:** Cartoon to illustrate the processes to explain the spatial association of magnetite and  
788 vesicles, and to show the effects of such an association on the fluid mechanics of magma mingling.  
789 Water-saturated basaltic magma underplates an andesite magma body. Bubbles nucleate on  
790 magnetite over other crystal phases (amphibole is likely also a liquidus phase). The low viscosity of  
791 the melt and the significant fraction of exsolved vapour allow bubbles to rise up to the interface  
792 between the two magmas, sweeping up magnetite grains in the process. Bubbles and magnetite  
793 aggregates accumulate at the interface between the two magmas. Instabilities at the interface allow  
794 mafic enclaves to form and become incorporated into the andesite body. The enclaves are enriched  
795 in both magnetite and bubbles relative to the bulk mafic magma at depth.

796

797

798

<i>Sample name</i>	<i>Description of sample</i>	<i>Size of pixel (micrometers) in analysed BSE image</i>
BR6a 1	Mafic enclave; glassy groundmass and quenched margins; 1 closest to rim, 3 closest to core (Type A)	2.15
BR6a 2		1.46
BR6a 3		
BR10 1	Mafic enclave; crystalline groundmass, no quenched margins (Type B)	2.22
BR10 2		
BR11 1	Mafic enclave; partially crystalline groundmass, quenched margins (Type A)	2.22
BR11 2		1.11
BR 12 1	Mafic enclave; glassy groundmass and quenched margins (Type A)	1.11
BR 12 2		
BR 12 3		
MT19 1	Mafic enclave; glassy groundmass and quenched margins (Type A)	0.24
MT19 2	Andesite	0.12
MT19 3	Andesite	
MT19 4	Andesite	
MVO 1560 1	Andesite	0.24
MVO 1560 2	Andesite	0.12
MVO 1560 3	Andesite	0.24
MVO 1560 4	Mafic enclave; crystalline groundmass, no quenched margins (Type B)	
MVO 1587 1	Mafic enclave; crystalline groundmass, no quenched margins (Type B)	
MVO 1587 2	Andesite	
MVO 1592 1	Mafic enclave; crystalline groundmass, no quenched margins (Type B)	0.12
MVO 1592 2	Andesite	
MVO 1592 3	Andesite	
MVO 1592 4	Mafic enclave; crystalline groundmass, no quenched margins (Type B)	0.24

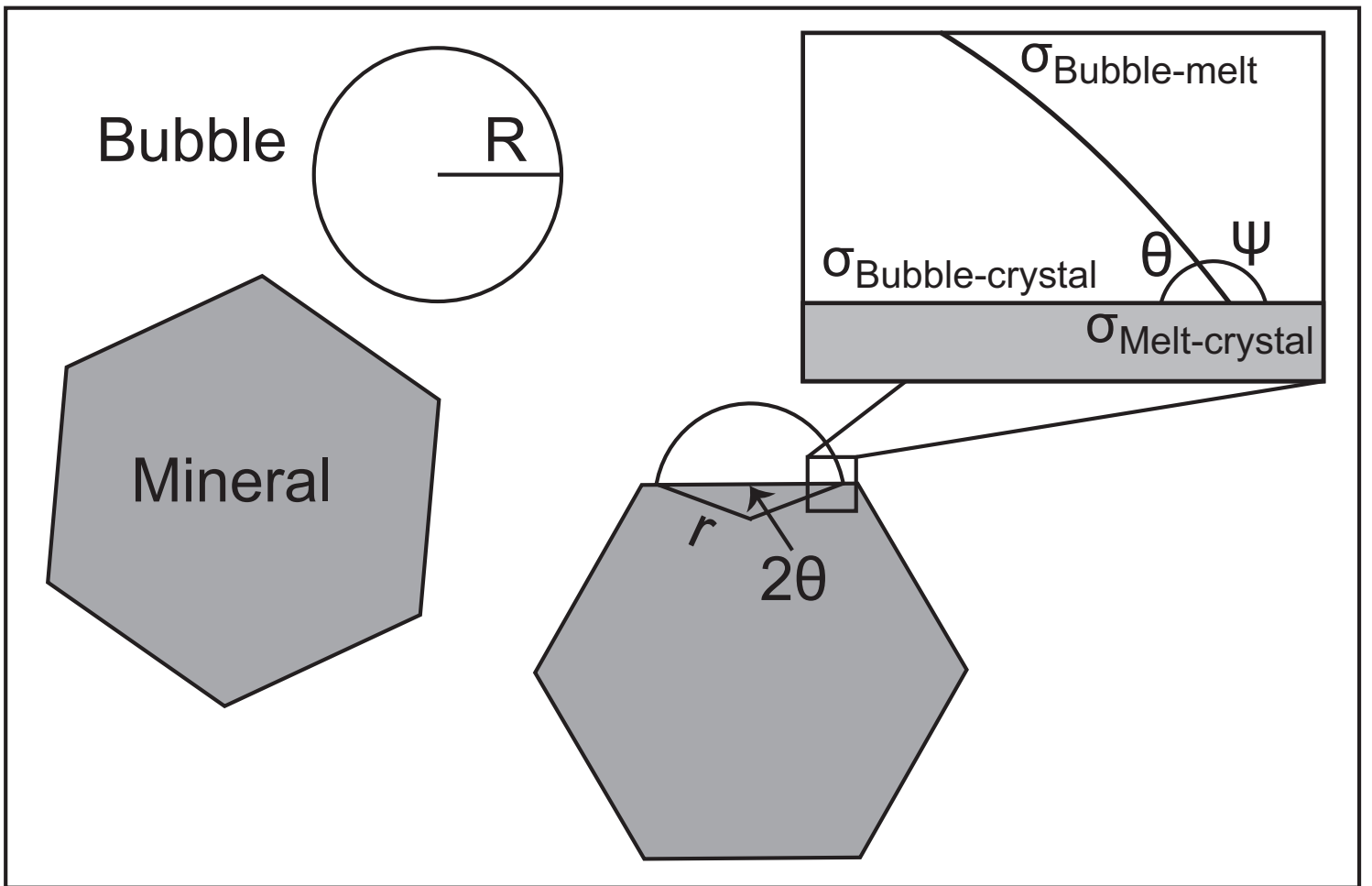
817

818

819 **Table 1:** Sample names, types (andesite or mafic enclave) and brief description. See text for  
 820 descriptions of andesite and mafic enclave petrography. Types A and B after Plail et al. (2014).

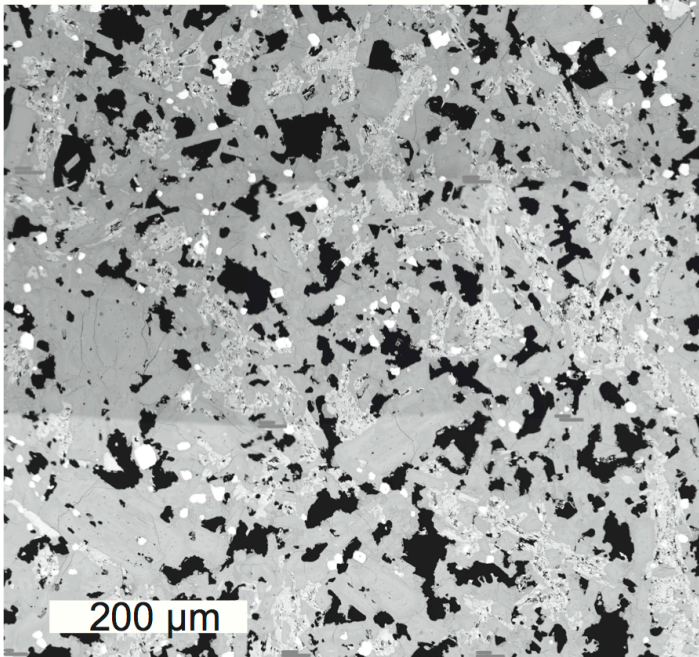
821

822

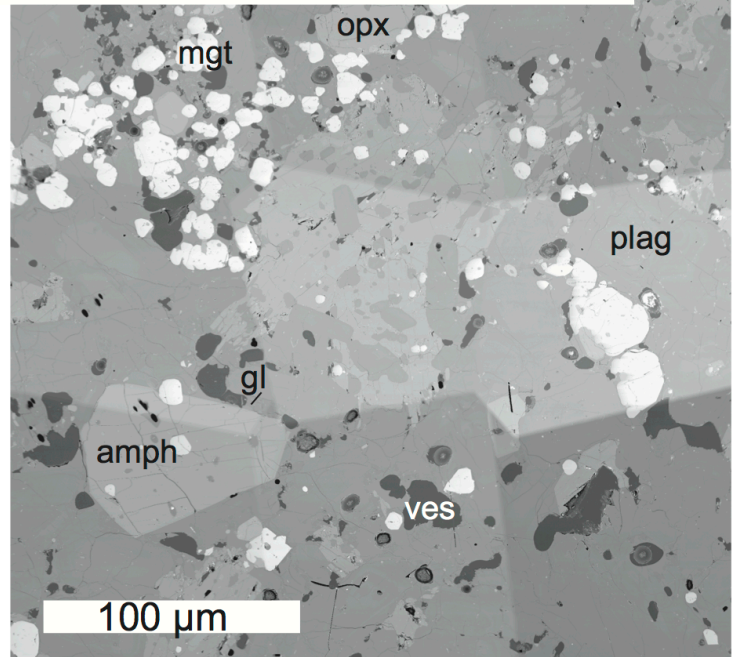




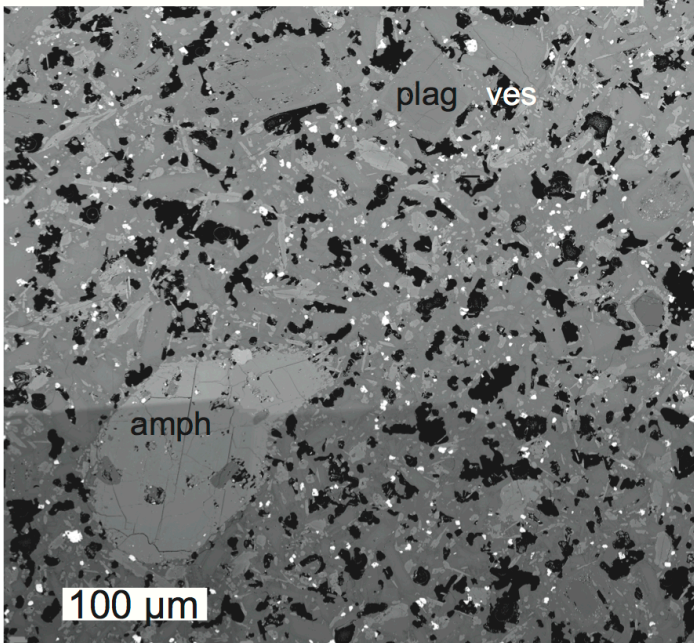
a: mafic enclave MVO 1587\_1



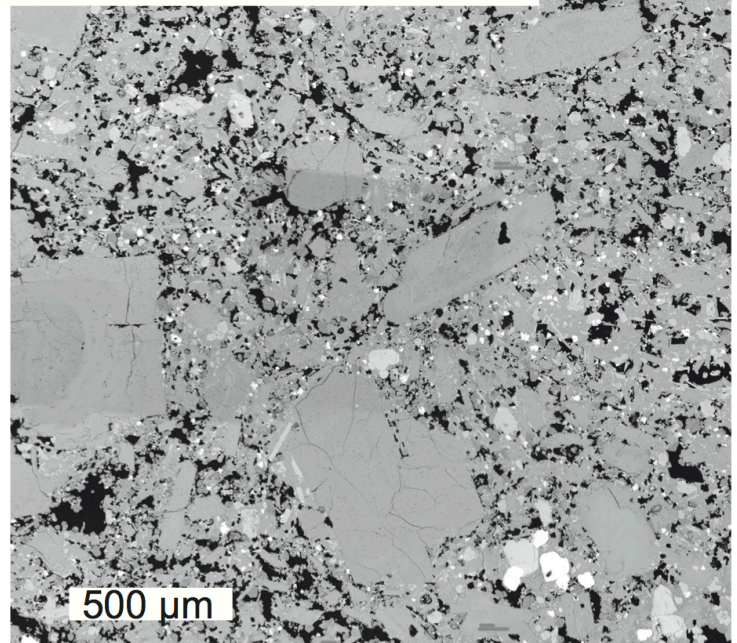
b: MT19\_1 mafic enclave



c: mafic enclave MVO 1592\_4

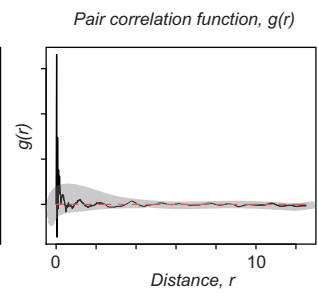
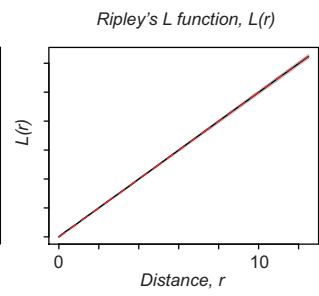
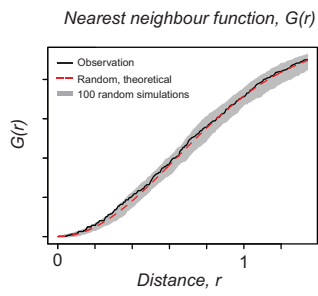
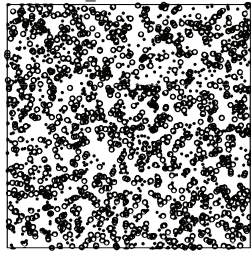


d: andesite MVO 1592\_2

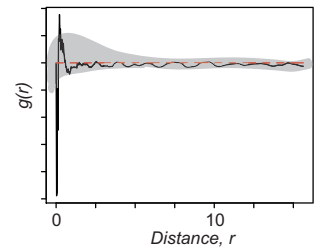
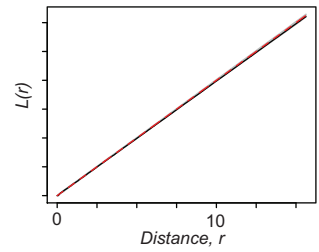
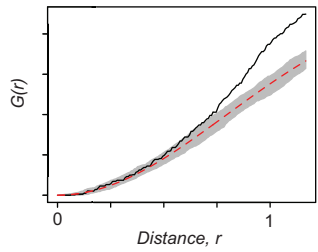
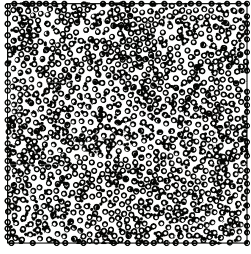


**Independent populations**

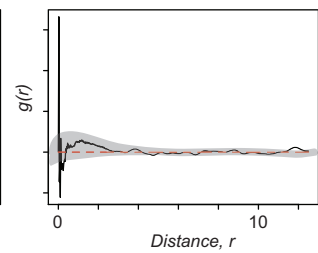
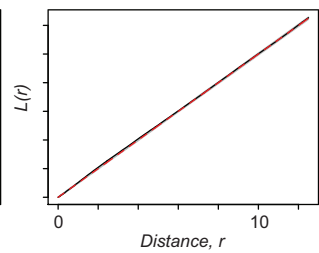
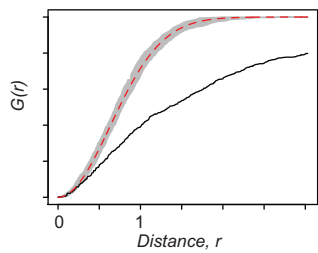
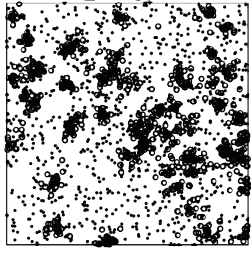
*a. random\_random*



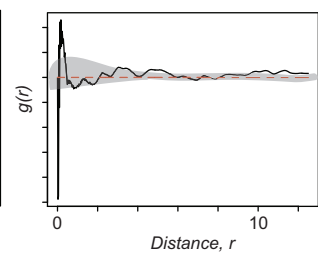
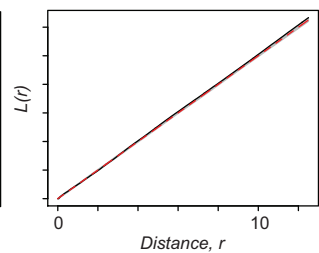
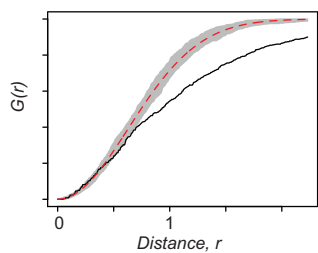
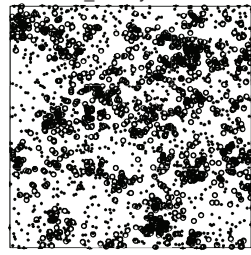
*b. random\_ordered*



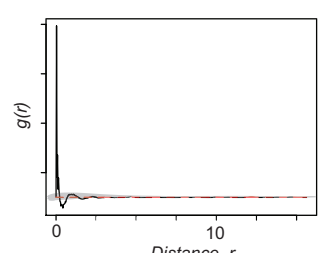
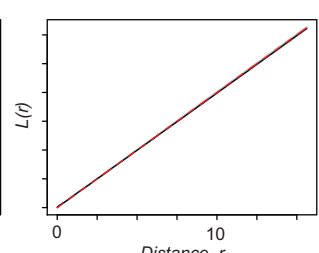
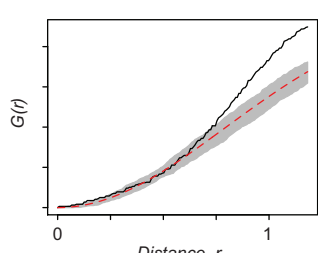
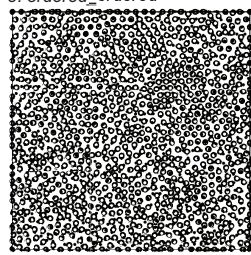
*c. random\_strongly clustered*



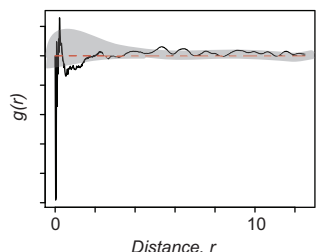
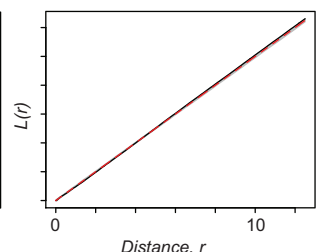
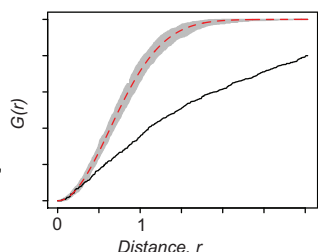
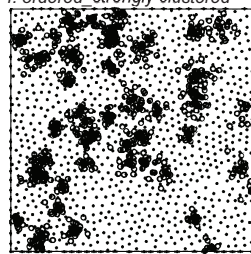
*d. random\_weakly clustered*



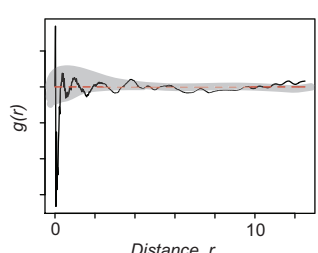
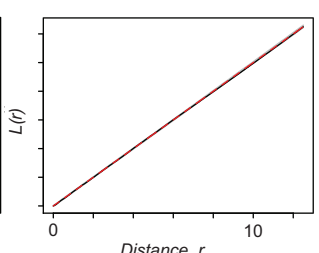
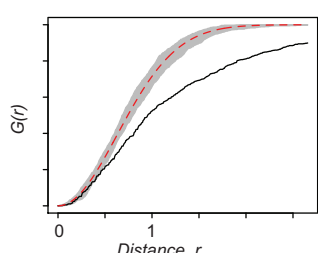
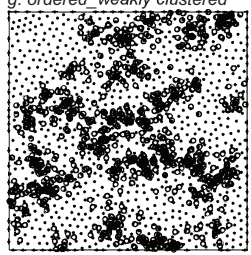
*e. ordered\_ordered*



*f. ordered\_strongly clustered*



*g. ordered\_weakly clustered*



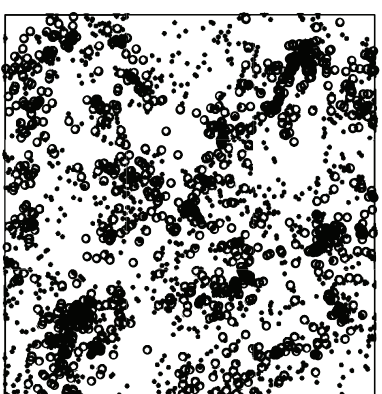
Independent populations, cont.

*h.* weakly-clustered\_weakly-clustered

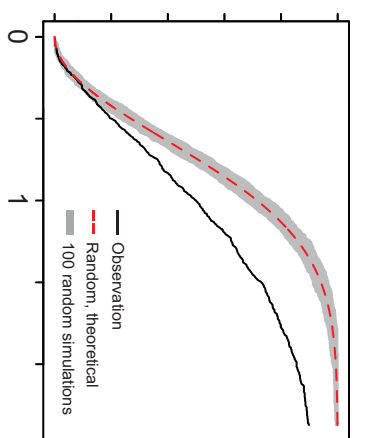
Nearest neighbour function,  $G(r)$

Ripley's L function,  $L(r)$

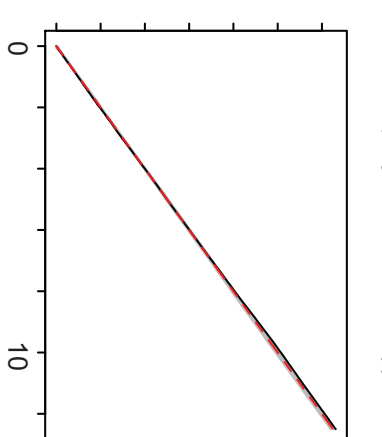
Pair correlation function,  $g(r)$



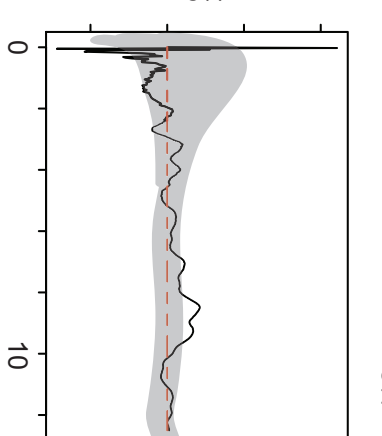
$G(r)$



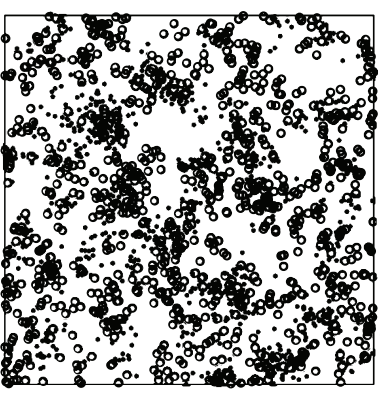
$L(r)$



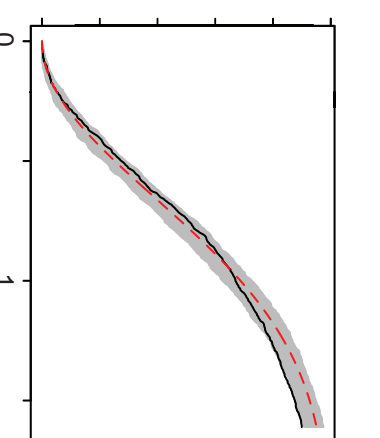
$g(r)$



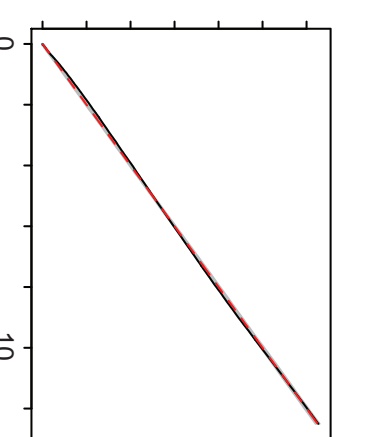
*i.* strongly-clustered\_weakly-clustered



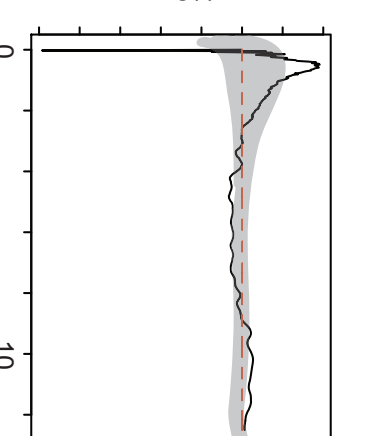
$G(r)$



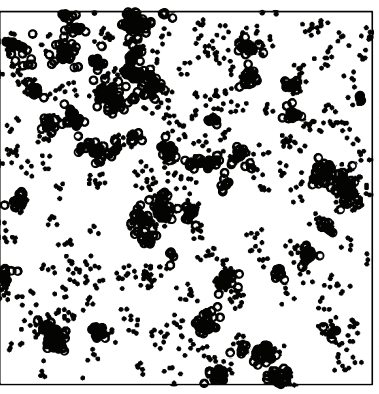
$L(r)$



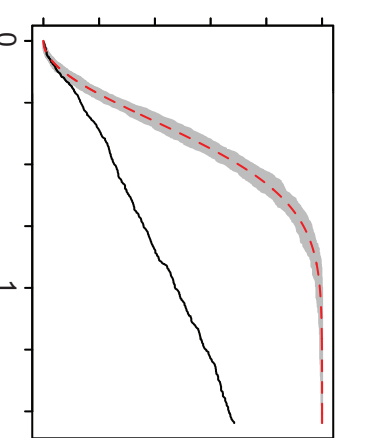
$g(r)$



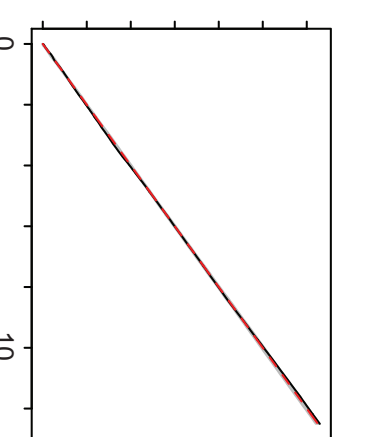
*j.* strongly-clustered\_strongly-clustered



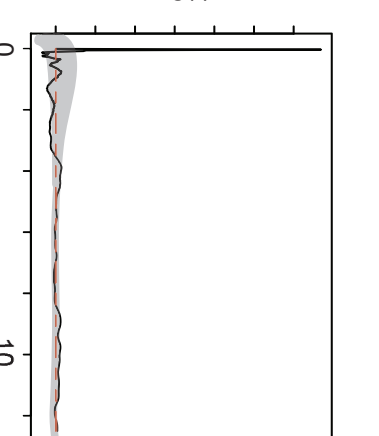
$G(r)$



$L(r)$



$g(r)$



— Observation  
- - - Random, theoretical  
■ 100 random simulations

Distance,  $r$

Distance,  $r$

Distance,  $r$

$L(r)$

$L(r)$

$L(r)$

Distance,  $r$

Distance,  $r$

Distance,  $r$

$g(r)$

$g(r)$

$g(r)$

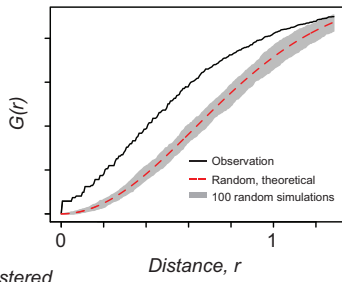
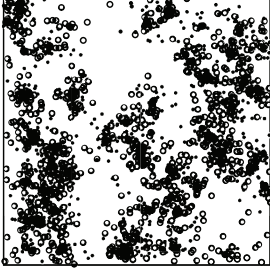
Distance,  $r$

Distance,  $r$

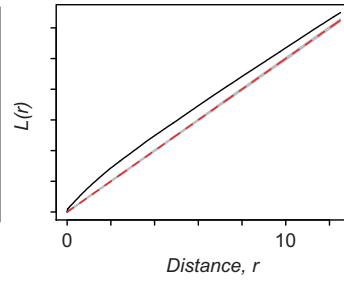
Distance,  $r$

**Dependent populations**

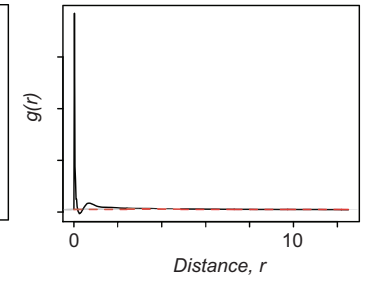
*a. weakly-clustered\_ weakly-clustered*      Nearest neighbour function,  $G(r)$



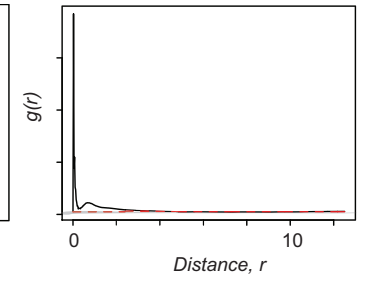
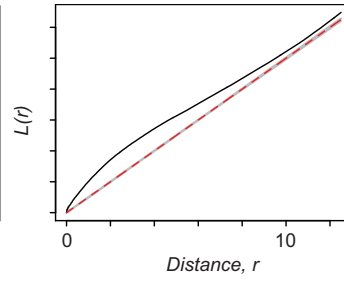
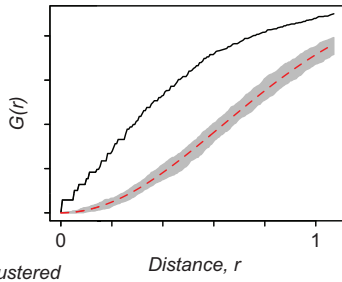
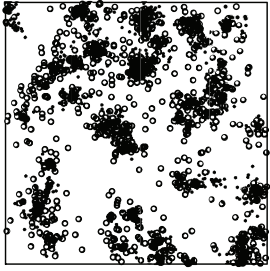
Ripley's L function,  $L(r)$



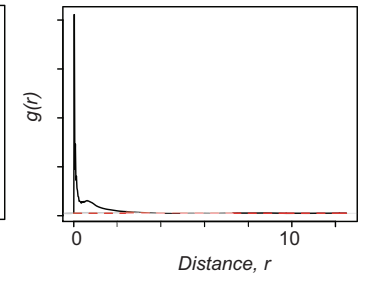
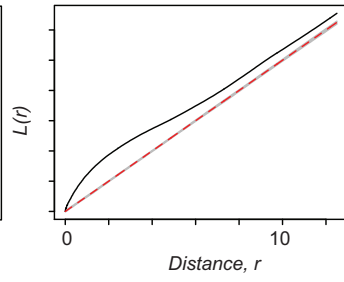
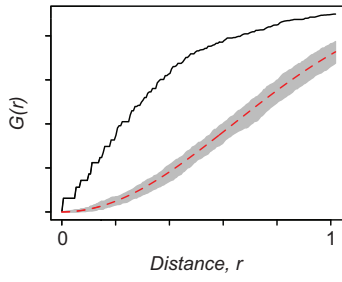
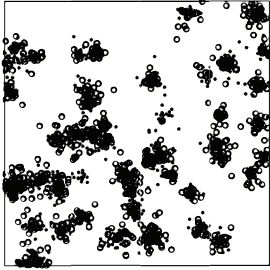
Pair correlation function,  $g(r)$



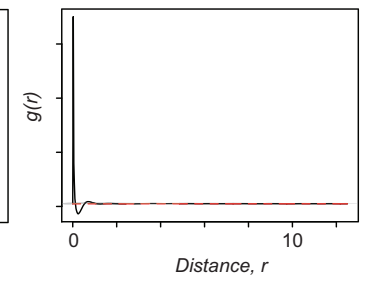
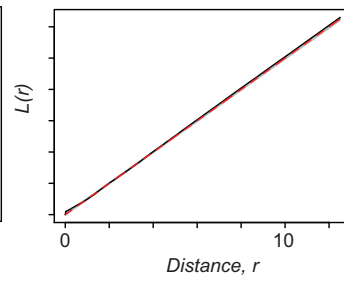
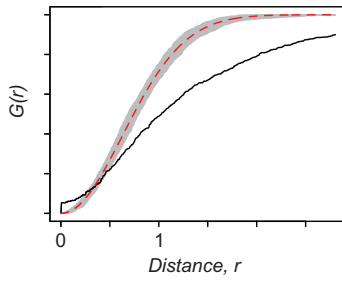
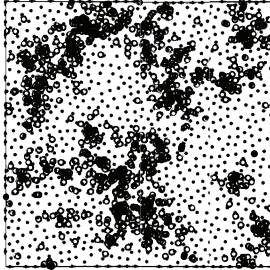
*b. strongly-clustered\_ weakly-clustered*



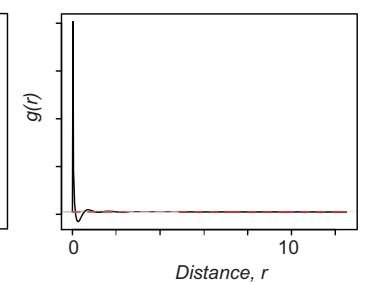
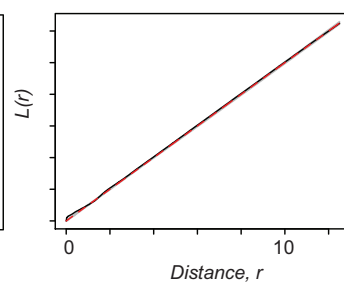
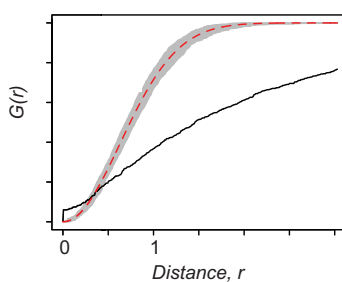
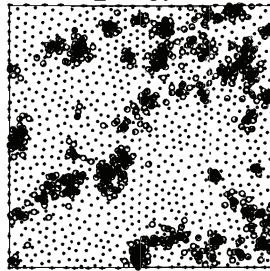
*c. strongly-clustered\_ strongly-clustered*



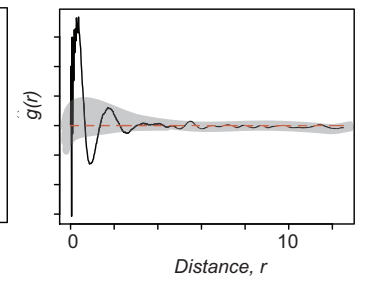
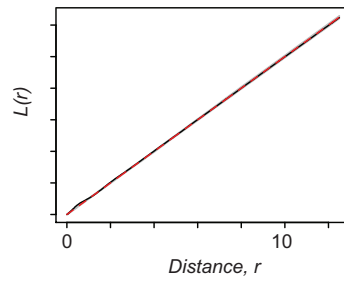
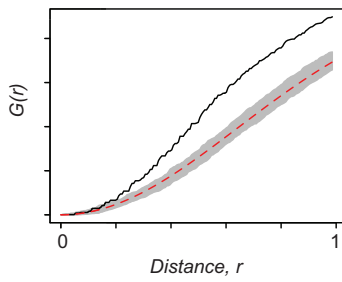
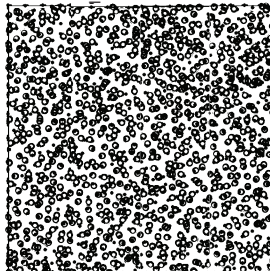
*d. ordered\_ weakly-clustered*



*e. ordered\_ strongly-clustered*

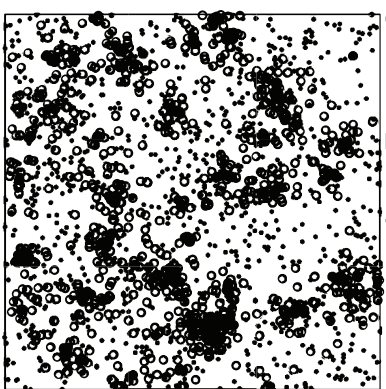


*f. ordered\_ randomised*

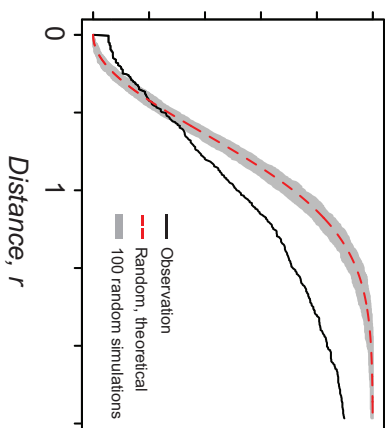


Dependent populations, cont.

*g. random weakly-clustered*

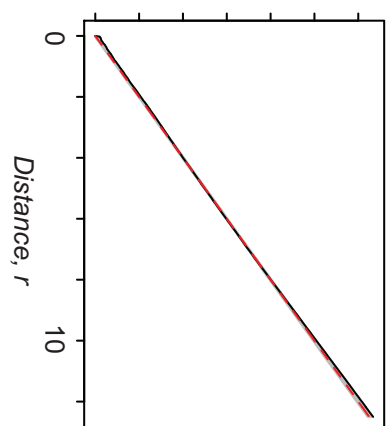


$G(r)$

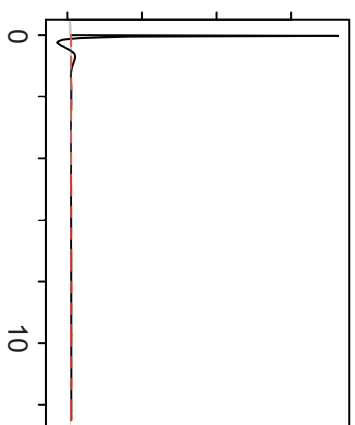


Nearest neighbour function,  $G(r)$

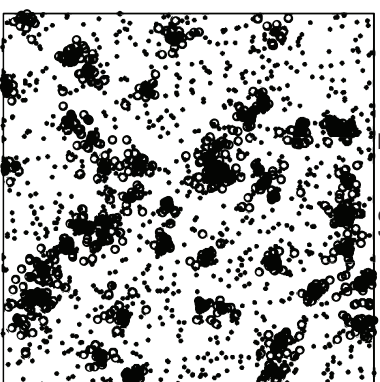
Ripley's L function,  $L(r)$



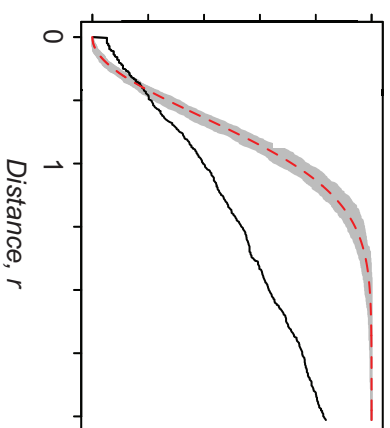
Pair correlation function,  $g(r)$



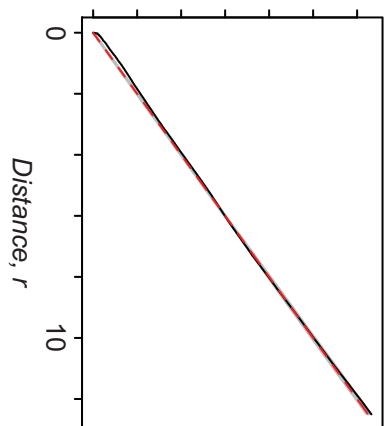
*h. random strongly-clustered*



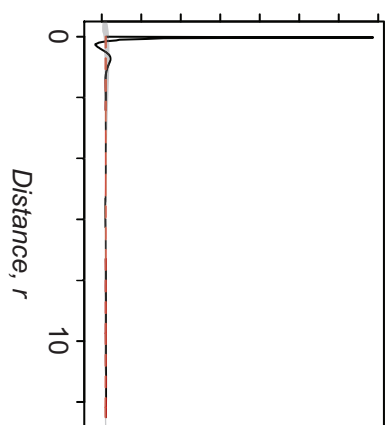
$G(r)$



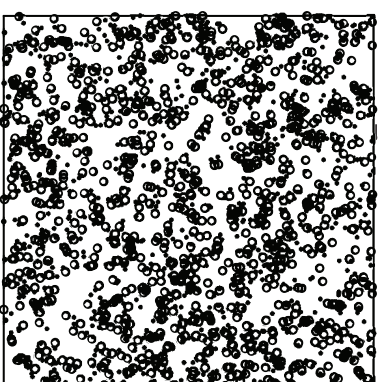
$L(r)$



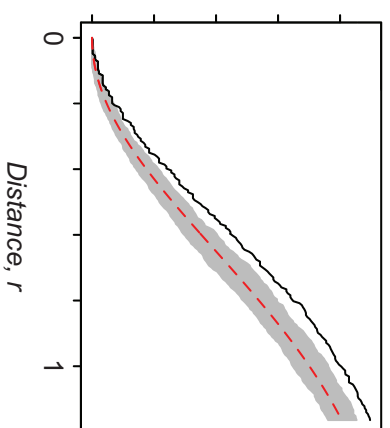
$g(r)$



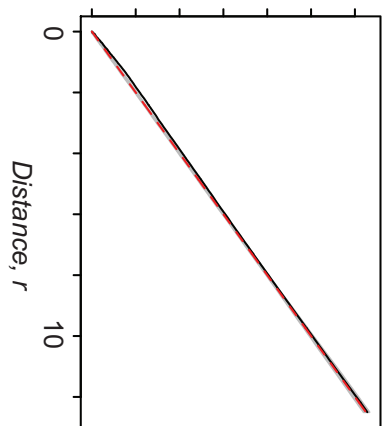
*i. random randomised*



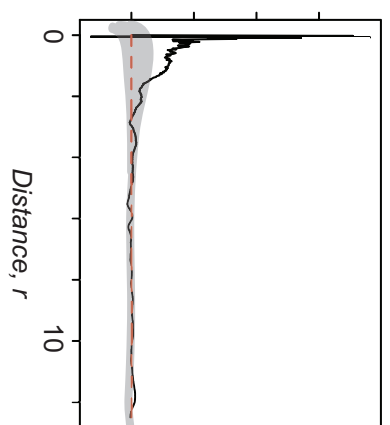
$G(r)$



$L(r)$



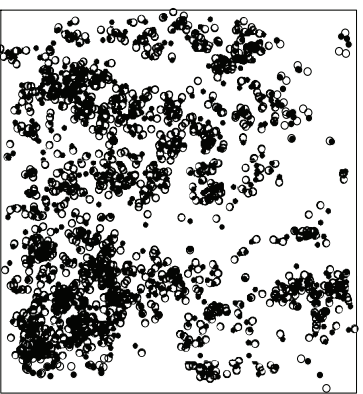
$g(r)$



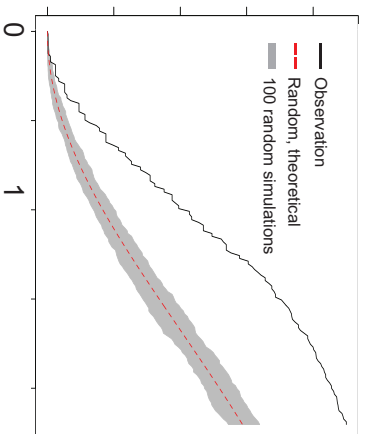
## Dependent populations - changing the order of the analysis

### a. weakly-clustered\_randomised

e.g. bubbles nucleating on clustered magnetites

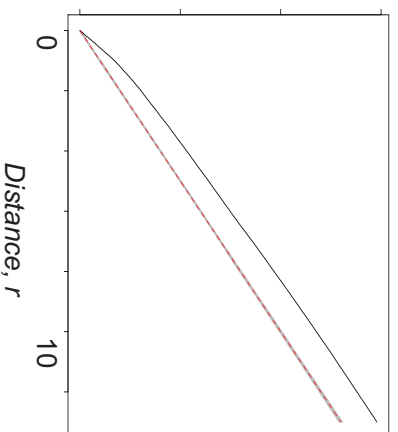


$G(r)$



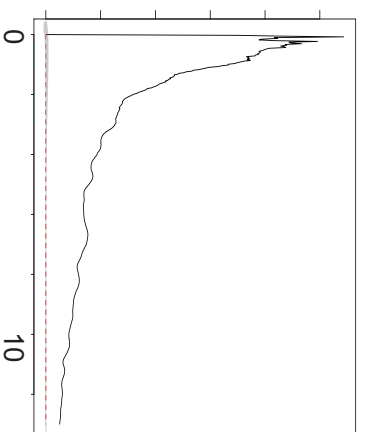
Nearest neighbour function,  $G(r)$

$L(r)$



Ripley's L function,  $L(r)$

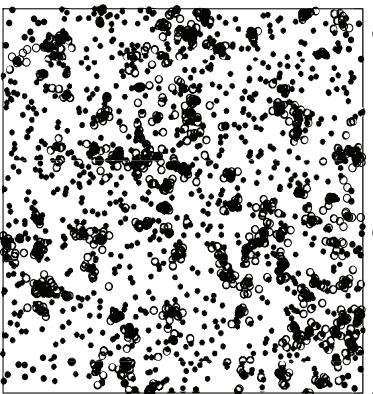
$g(r)$



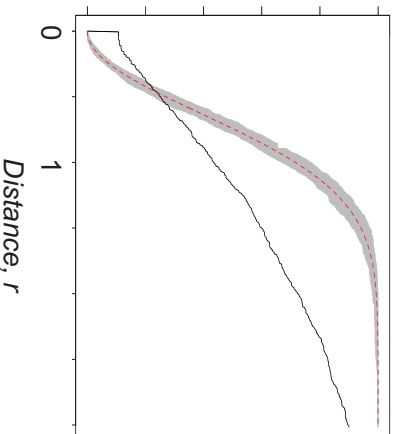
Pair correlation function,  $g(r)$

### b. random\_weakly-clustered

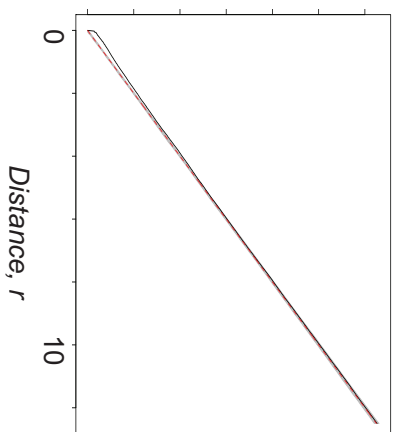
e.g. bubbles nucleating on random magnetites



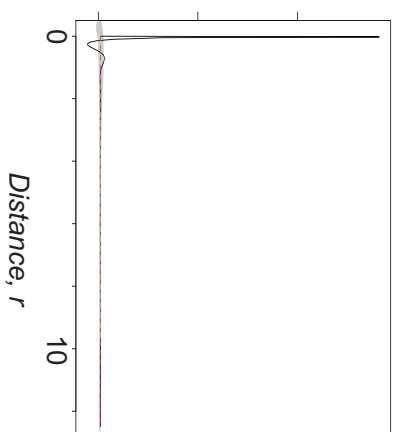
$G(r)$

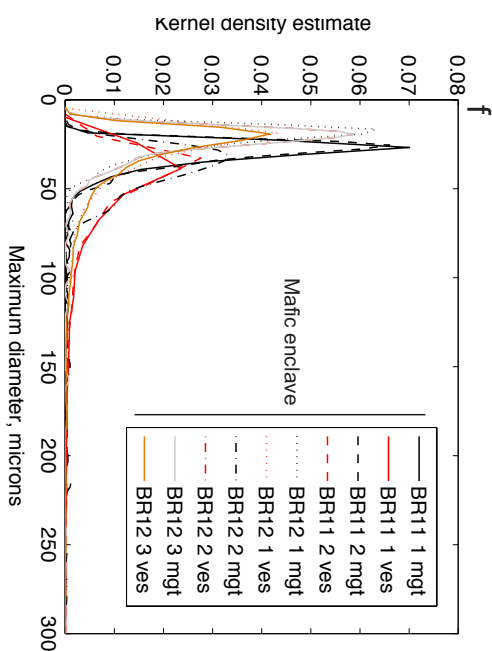
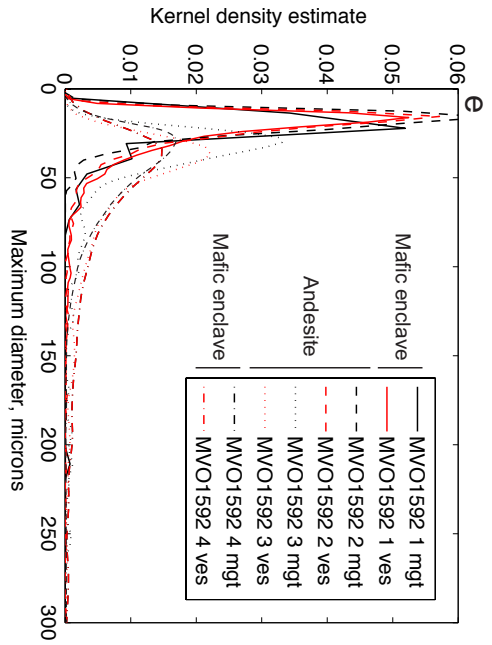
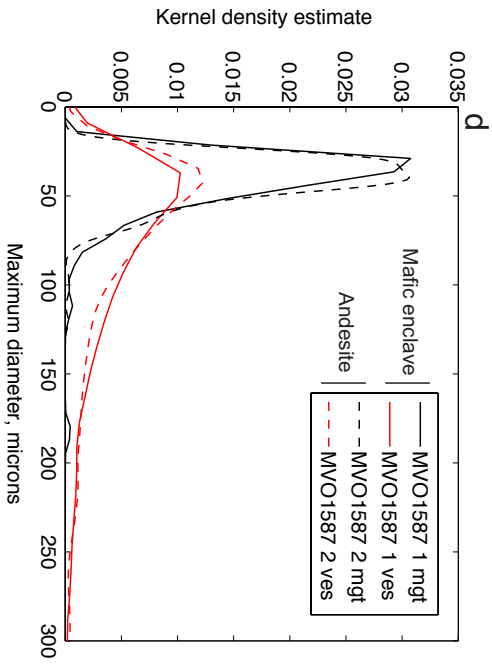
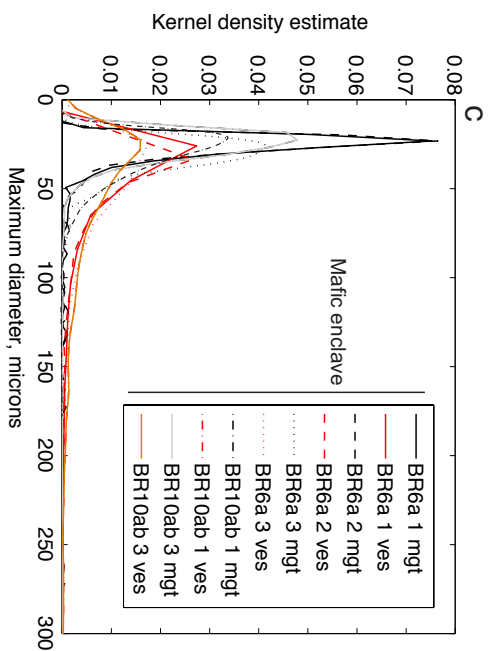
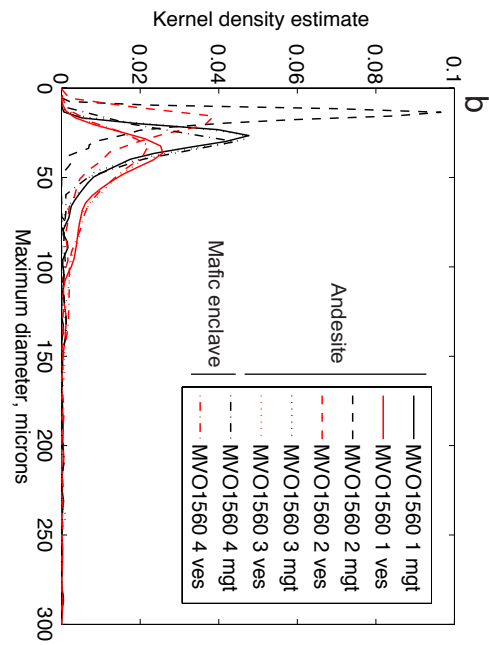
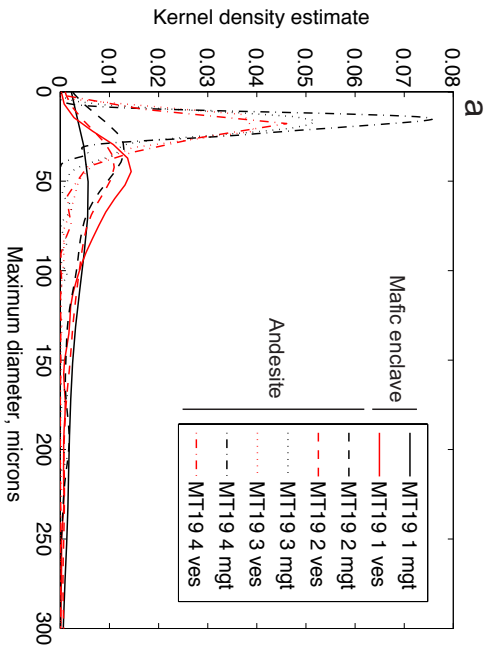


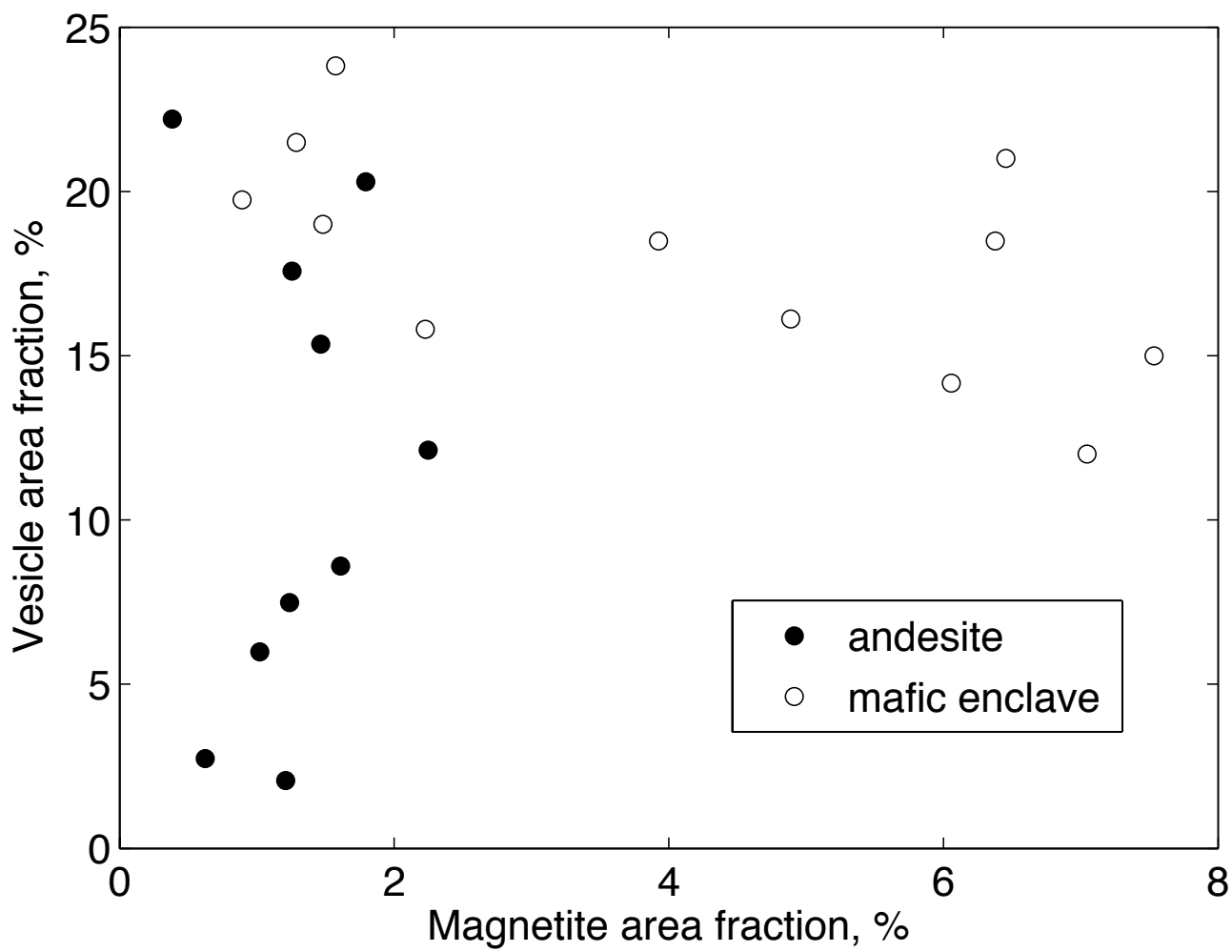
$L(r)$



$g(r)$

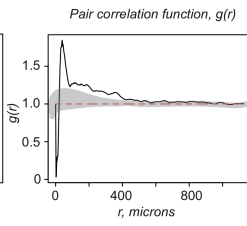
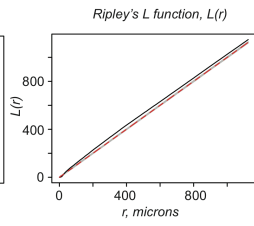
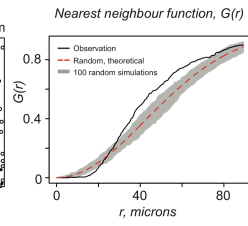
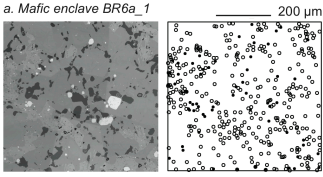




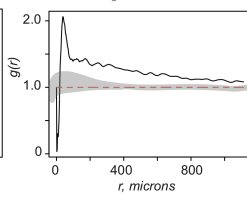
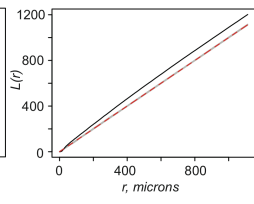
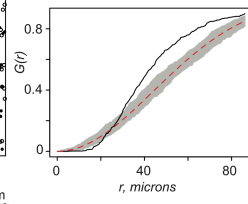
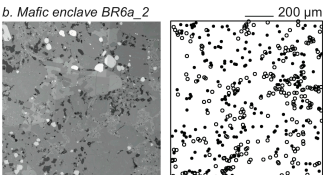




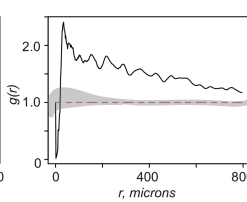
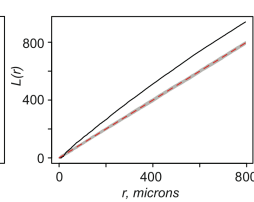
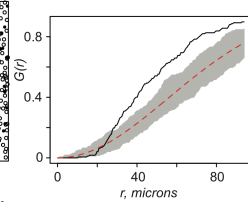
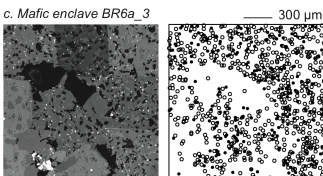
a. Mafic enclave BR6a\_1



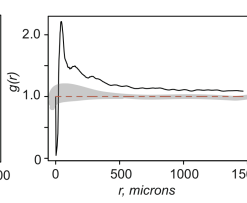
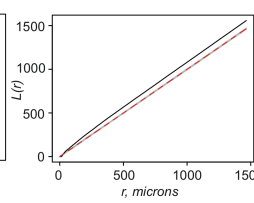
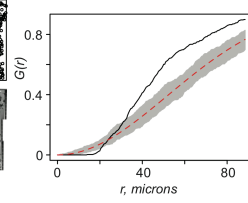
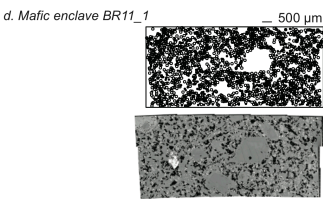
b. Mafic enclave BR6a\_2



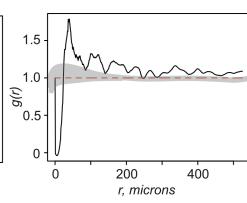
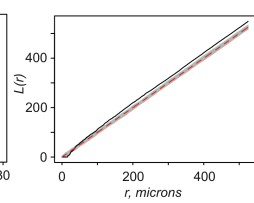
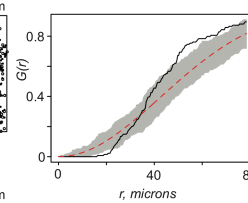
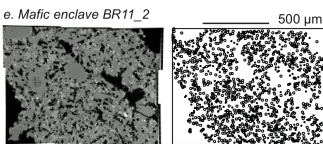
c. Mafic enclave BR6a\_3



d. Mafic enclave BR11\_1



e. Mafic enclave BR11\_2



f. Mafic enclave MVO 1587 1

